MNRAS **440,** 2692–2713 (2014) doi:10.1093/mnras/stu342

The clustering of galaxies in the SDSS-III Baryon Oscillation Spectroscopic Survey: cosmological implications of the full shape of the clustering wedges in the data release 10 and 11 galaxy samples

Ariel G. Sánchez,[1⋆] Francesco Montesano,[1] Eyal A. Kazin,[2,3] Eric Aubourg,[4] Florian Beutler,[5] Jon Brinkmann,[6] Joel R. Brownstein,[7] Antonio J. Cuesta,[8,9] Kyle S. Dawson,[7] Daniel J. Eisenstein,[10] Shirley Ho,[11,12] Klaus Honscheid,[13] Marc Manera,[14,15] Claudia Maraston,[15] Cameron K. McBride,[10] Will J. Percival,[15] Ashley J. Ross,[15] Lado Samushia,[15,16] David J. Schlegel,[5] Donald P. Schneider,[17,18] Ramin Skibba,[19] Daniel Thomas,[15] Jeremy L. Tinker,[20] Rita Tojeiro,[15] David A. Wake,[21,22] Benjamin A. Weaver,[20] Martin White[5,23] and Idit Zehavi[24]

[1]*Max-Planck-Institut für extraterrestrische Physik, Postfach 1312, Giessenbachstr., D-85741 Garching, Germany*
[2]*Centre for Astrophysics and Supercomputing, Swinburne University of Technology, PO Box 218, Hawthorn, Victoria 3122, Australia*
[3]*ARC Centre of Excellence for All-sky Astrophysics (CAASTRO), 44 Rosehill Street, Redfern, NSW 2016, Australia*
[4]*APC, University of Paris Diderot, CNRS/IN2P3, CEA/IRFU, Observatoire de Paris, Sorbonne Paris Cité, France*
[5]*Lawrence Berkeley National Laboratory, 1 Cyclotron Rd, Berkeley, CA 94720, USA*
[6]*Apache Point Observatory, PO Box 59, Sunspot, NM 88349-0059, USA*
[7]*Department of Physics and Astronomy, University of Utah, 115 S 1400 E, Salt Lake City, UT 84112, USA*
[8]*Institut de Ciències del Cosmos, Universitat de Barcelona, IEEC-UB, Martí Franquès 1, E08028 Barcelona, Spain*
[9]*Department of Physics, Yale University, 260 Whitney Ave, New Haven, CT 06520, USA*
[10]*Harvard–Smithsonian Center for Astrophysics, 60 Garden St., Cambridge, MA 02138, USA*
[11]*Department of Physics, Carnegie Mellon University, 5000 Forbes Ave., Pittsburgh, PA 15213, USA*
[12]*McWilliams Center for Cosmology, Carnegie Mellon University, 5000 Forbes Avenue, Pittsburgh, PA 15213, USA*
[13]*Department of Physics and Center for Cosmology and Astro-Particle Physics, Ohio State University, Columbus, Ohio 43210, USA*
[14]*University College London, Gower Street, London WC1E 6BT, UK*
[15]*Institute of Cosmology & Gravitation, University of Portsmouth, Dennis Sciama Building, Portsmouth PO1 3FX, UK*
[16]*National Abastumani Astrophysical Observatory, Ilia State University, 2A Kazbegi Ave., GE-1060 Tbilisi, Georgia*
[17]*Department of Astronomy and Astrophysics, The Pennsylvania State University, University Park, PA 16802, USA*
[18]*Institute for Gravitation and the Cosmos, The Pennsylvania State University, University Park, PA 16802, USA*
[19]*Steward Observatory, University of Arizona, 933 N. Cherry Ave., Tucson, AZ 85721, USA*
[20]*Center for Cosmology and Particle Physics, New York University, New York, NY 10003, USA*
[21]*Department of Astronomy, University of Wisconsin-Madison, 475 N. Charter Street, Madison, WI 53706, USA*
[22]*Department of Physical Sciences, The Open University, Milton Keynes, MK7 6AA, UK*
[23]*Department of Physics, University of California Berkeley, CA 94720, USA*
[24]*Department of Astronomy, Case Western Reserve University, Cleveland, OH 44106, USA*

Accepted 2014 February 19. Received 2014 February 18; in original form 2013 December 17

ABSTRACT

We explore the cosmological implications of the angle-averaged correlation function, $\xi(s)$, and the clustering wedges, $\xi_\perp(s)$ and $\xi_\parallel(s)$, of the LOWZ and CMASS galaxy samples from Data Releases 10 and 11 of the Sloan Digital Sky Survey III (SDSS-III) Baryon Oscillation Spectroscopic Survey. Our results show no significant evidence for a deviation from the standard Λ cold dark matter model. The combination of the information from our clustering measurements with recent data from the cosmic microwave background is sufficient to constrain the curvature of the Universe to $\Omega_k = 0.0010 \pm 0.0029$, the total neutrino mass to $\sum m_\nu < 0.23\,\mathrm{eV}$ (95 per cent confidence level), the effective number of relativistic species to $N_{\mathrm{eff}} = 3.31 \pm 0.27$

⋆ E-mail: arielsan@mpe.mpg.de

and the dark energy equation of state to $w_{\rm DE} = -1.051 \pm 0.076$. These limits are further improved by adding information from Type Ia supernovae and baryon acoustic oscillations from other samples. In particular, this data set combination is completely consistent with a time-independent dark energy equation of state, in which case we find $w_{\rm DE} = -1.024 \pm 0.052$. We explore the constraints on the growth rate of cosmic structures assuming $f(z) = \Omega_{\rm m}(z)^{\gamma}$ and obtain $\gamma = 0.69 \pm 0.15$, consistent with the predictions of general relativity of $\gamma = 0.55$.

Key words: cosmological parameters – large-scale structure of Universe.

1 INTRODUCTION

The large-scale distribution of galaxies contains the signature of acoustic waves that propagated through the Universe prior to the epoch of recombination. This signal, referred to as baryon acoustic oscillations (BAO), appears as a modulation in the amplitude of the galaxy power spectrum, $P(k)$, and a broad peak in the large-scale two-point correlation function, $\xi(s)$ (Eisenstein & Hu 1998; Meiksin, White & Peacock 1999; Matsubara 2004). The wavelength of the oscillations in $P(k)$ and the location of the peak in $\xi(s)$ can be associated with the maximum distance that these acoustic waves can travel before the decoupling of matter and radiation, that is, the sound horizon at the drag redshift, $r_{\rm d}$. As this scale can be constrained with high accuracy from observations of the cosmic microwave background (CMB), the acoustic scale inferred from the clustering of galaxy samples at different redshifts can be used as a standard ruler to measure the distance–redshift relation, providing a powerful and robust probe of the expansion history of the Universe (Blake & Glazebrook 2003; Linder 2003; Seo & Eisenstein 2003).

The BAO signal was first detected in the clustering of the Two-degree Field Galaxy Redshift survey (Colless et al. 2001, 2003) by Cole et al. (2005) and the luminous red galaxy (LRG; Eisenstein et al. 2001) sample of the Sloan Digital Sky Survey (SDSS; York et al. 2000) by Eisenstein et al. (2005). Since then, subsequent analyses on various galaxy samples have provided BAO measurements with increasing precision (Padmanabhan et al. 2007; Beutler et al. 2011; Blake et al. 2011; Anderson et al. 2012, 2014; Seo et al. 2012; Xu et al. 2012). Using these results it is now possible to construct a Hubble diagram based entirely on BAO distance measurements. It has become standard practice to use this information, in combination with additional data sets, when deriving constraints on cosmological parameters.

Separate measurements of the acoustic scale in the directions parallel and perpendicular to the line of sight can be used to obtain constraints on the Hubble parameter, $H(z)$, and the angular diameter distance, $D_{\rm A}(z)$, through the Alcock–Paczynski test (Alcock & Paczynski 1979; Hu & Haiman 2003). However, the BAO signal on angle-averaged clustering measurements such as $P(k)$ or $\xi(s)$ provides estimates of the average distance $D_{\rm V}(z) \propto D_{\rm A}(z)^2/H(z)$. Although most analyses have focused on angle-averaged quantities, the large volumes probed by present-day galaxy samples make it possible to extend these analyses to anisotropic clustering measurements (Cabré & Gaztañaga 2009; Blake et al. 2012; Xu et al. 2012; Anderson et al. 2014; Kazin et al. 2013) using the full power of the BAO test.

The clustering of galaxies encodes additional information beyond that contained in the BAO signal that can significantly improve the cosmological constraints derived from large-scale structure (LSS) data sets. This extra information is particularly important for anisotropic clustering measurements, where the signature of the so-called redshift-space distortions (RSD) can be used to constrain the growth rate of cosmic structures (Guzzo et al. 2008). In this way, anisotropic clustering measurements can provide information of the expansion history of the Universe and the growth of density fluctuations, which can be used to distinguish between the dark energy and modified gravity scenarios for the origin of cosmic acceleration.

The most accurate BAO measurements to date have been obtained from the Baryon Oscillation Spectroscopic Survey (BOSS; Dawson et al. 2013), which is one of the four component surveys of SDSS-III (Eisenstein et al. 2011). After applying a modified version of the reconstruction technique of Eisenstein et al. (2007), the BAO signal in the galaxy clustering of BOSS SDSS Data Release 9 (DR9; Ahn et al. 2012) provided a 1.7 per cent accuracy measurement of the average distance $D_{\rm V}(z)$ at $z = 0.57$ (Anderson et al. 2012), as well as separate constraints on $D_{\rm A}(z)$ and $H(z)$ at the same redshift with 3 and 8 per cent accuracy, respectively (Anderson et al. 2014). These measurements have been complemented by analyses of the full shape of isotropic and anisotropic clustering measurements (Reid et al. 2012; Sánchez et al. 2012, 2013; Chuang et al. 2013a; Samushia et al. 2013a). Besides galaxy clustering analyses, a sample of high-redshift quasars from BOSS has been used to detect for the first time the signature of the BAO in the fluctuations of the Lyman α forest at $z \simeq 2.4$ (Busca et al. 2013; Slosar et al. 2013).

In this paper, we use information from the full shape of the two-point correlation function and the clustering wedges statistic (Kazin, Sánchez & Blanton 2012) measured from BOSS data to derive constraints on cosmological parameters. We extend the analyses of Sánchez et al. (2012, 2013) based on a high-redshift galaxy sample from BOSS DR9 to the data corresponding to DR10 (Ahn et al. 2013) and DR11 (internal data release), including results from the low-redshift BOSS galaxy sample.

As the statistical uncertainties characterizing different cosmological observations become smaller, it is important to explore potential systematics that can be introduced by the analysis techniques and models applied to the data. The comparison of the results obtained by applying multiple methods to the same data can be used to identify the presence of systematic errors. Our analysis is part of a series of papers examining the clustering properties of the BOSS DR10 and DR11 galaxy samples with different methodologies. Tojeiro et al. (2014) and Anderson et al. (2013) analyse the isotropic and anisotropic BAO signal in these samples and explore their cosmological implications. Ross et al. (2014) study the sensitivity of these BAO measurements to the properties of the galaxy population being analysed. Vargas-Magaña et al. (2013) investigate the potential systematic errors affecting anisotropic BAO measurements. Percival et al. (2014) perform a detailed analysis of the effect of the uncertainties in the covariance matrices determined from mock catalogues on the obtained constraints. These analyses are complemented by those of Chuang et al. (2013b), Samushia et al. (2014) and Beutler et al. (2013), who analyse the full shape of the monopole–quadrupole pair in configuration and Fourier space. These studies attempt to condense the information of the clustering

measurements into a few numbers reflecting the geometric constraints and the measurements of the growth of structures, which are then compared with the predictions from different cosmological models. We follow an alternative approach in which we perform the comparison with cosmological models at the level of the galaxy clustering measurements themselves. The consistency of the results presented here and those of our companion papers is a reassuring indication of the robustness of our results.

The outline of this paper is as follows. In Section 2, we describe our galaxy sample, the procedure followed to obtain our clustering measurements and their respective covariance matrices, as well as the additional data sets included in our analysis. In Section 3, we review our model of the full shape of the correlation function and the clustering wedges and our methodology to obtain cosmological constraints. In Section 4, we present the constraints on cosmological parameters obtained from different combinations of data sets and parameter spaces. Finally, Section 5 contains our main conclusions.

Throughout the paper, we assume a flat Λ cold dark matter (ΛCDM) fiducial cosmological model with matter density, in units of the critical density, of $\Omega_{\rm m} = 0.274$, a Hubble parameter $h = 0.7$ (expressed in units of $100\,{\rm km\,s^{-1}\,Mpc^{-1}}$), a baryon density of $\Omega_{\rm b}h^2 = 0.0224$, a scalar spectral index of $n_{\rm s} = 0.95$ and a linear-theory rms mass fluctuation in spheres of radius $8\,h^{-1}\,{\rm Mpc}$ of $\sigma_8 = 0.8$. This choice matches the fiducial cosmology assumed by Anderson et al. (2013).

2 THE DATA

2.1 The Baryon Oscillation Spectroscopic Survey

2.1.1 Galaxy clustering measurements from BOSS

We use the LOWZ and CMASS samples of BOSS corresponding to SDSS DR10 (Ahn et al. 2013) and DR11, which will become publicly available with the final data release of the survey. These galaxy samples were selected on the basis of the SDSS multicolour photometric observations (Gunn et al. 1998, 2006) to cover the redshift range $0.15 < z < 0.7$ with a roughly uniform comoving number density $n \simeq 3 \times 10^{-4}\,h^3\,{\rm Mpc}^{-3}$ (Eisenstein et al. 2011; Dawson et al. 2013; Padmanabhan et al., in preparation). Up to ~30 and 2 per cent of LOWZ and CMASS targets, respectively, were observed during the SDSS I/II surveys (York et al. 2000) and thus already have a redshift. The remaining redshifts were measured from the spectra obtained with the double-armed BOSS spectrographs (Smee et al. 2013) by applying the minimum-χ^2 template-fitting procedure described in Aihara et al. (2011) and Bolton et al. (2012).

The LOWZ sample consists primarily of red galaxies that lie in massive haloes, with a satellite fraction of 12 per cent (Parejko et al. 2013). The CMASS sample is approximately complete down to a limiting stellar mass of $M \simeq 10^{11.3}\,{\rm M}_\odot$ (Maraston et al. 2013), and has an ~10 per cent satellite fraction (White et al. 2011; Nuza et al. 2013). Although this sample is dominated by early-type galaxies, it contains a significant fraction of massive spirals (~26 per cent; Masters et al. 2011), with measurable star formation activity from their emission line spectra (Thomas et al. 2013). Anderson et al. (2013) describe the construction of catalogues for LSS analyses based on these samples. We use these samples separately, restricting our analysis to the redshift ranges $0.15 < z < 0.43$ for the LOWZ sample and $0.43 < z < 0.7$ for the CMASS galaxies. This results in 218 905 and 501 844 galaxies for the DR10 LOWZ and CMASS galaxy samples, respectively, and 313 780 and 690 826 galaxies for the corresponding DR11 data sets.

We study the clustering properties of these galaxy samples by means of the angle-averaged correlation function, $\xi(s)$, and the clustering wedges statistic (Kazin et al. 2012), $\xi_{\Delta\mu}(s)$. The latter corresponds to the average of the full two-dimensional correlation function $\xi(\mu, s)$, where μ is the cosine of the angle between the separation vector $\boldsymbol{s}$ and the line-of-sight direction, over the interval $\Delta\mu = \mu_{\rm max} - \mu_{\rm min}$, that is

$$\xi_{\Delta\mu}(s) \equiv \frac{1}{\Delta\mu}\int_{\mu_{\rm min}}^{\mu_{\rm max}} \xi(\mu, s)\,{\rm d}\mu. \quad (1)$$

We use two wide clustering wedges, $\xi_\perp(s)$ and $\xi_\parallel(s)$, defined for the intervals $0 \le \mu \le 0.5$ and $0.5 \le \mu \le 1$, respectively. The basic procedure implemented to obtain these measurements from the LOWZ and CMASS samples is analogous to that of Anderson et al. (2013) and Sánchez et al. (2013). Here we summarize the most important points and refer the reader to these studies for more details.

We assume our fiducial cosmology to convert the observed redshifts into distances. We use the estimator of Landy & Szalay (1993) to compute the full correlation function $\xi(\mu, s)$ of the LOWZ and CMASS samples, with random samples following the same selection function as the original catalogues but containing 50 times more objects. The value of μ of a given pair is defined as the cosine of the angle between the separation vector, $\boldsymbol{s}$, and the line-of-sight direction at the mid-point of $\boldsymbol{s}$. We infer the correlation function $\xi(s)$ and the clustering wedges $\xi_\perp(s)$ and $\xi_\parallel(s)$ by averaging the full $\xi(\mu, s)$ over the corresponding μ intervals. As discussed in Kazin et al. (2012), this procedure correctly accounts for the μ dependence of the random–random counts, which is ignored when the estimator of Landy & Szalay (1993) is applied to the averaged counts directly, leading to a bias in the recovered clustering measurements.

When computing the pair counts, we assign a series of weights to each object in our catalogue. First, we apply a radial weight designed to minimize the variance of our measurements (Feldman, Kaiser & Peacock 1994) given by

$$w_{\rm r} = \frac{1}{1 + P_w\bar{n}(z)}, \quad (2)$$

where $\bar{n}(z)$ is the expected number density of the catalogue at the given redshift and P_w is a scale-independent parameter, which we set to $P_w = 2 \times 10^4\,h^{-3}\,{\rm Mpc}^3$. We also include angular weights to account for redshift failures and fibre collisions. For the CMASS sample, we apply additional weights to correct for the systematic effect introduced by the local stellar density and the seeing of the observations, as described in detail in Anderson et al. (2013).

Figs 1 and 2 show clustering measurements from, respectively, DR10 and DR11. In each case, the left-hand panels show the angle-averaged $\xi(s)$, and the right-hand panels the clustering wedges. Upper panels show results from the LOWZ sample and the lower panels show CMASS measurements. The anisotropic clustering pattern generated by RSD leads to significant differences in the amplitude and shape of the two clustering wedges, with $\xi_\parallel(s)$ showing a lower amplitude and a stronger damping of the BAO peak than $\xi_\perp(s)$. The dashed lines in both figures correspond to the best-fitting ΛCDM model obtained from the combination of the LOWZ and CMASS DR11 clustering wedges with CMB observations from the *Planck* satellite (Planck Collaboration I 2013) and the CMB polarization measurements from *Wilkinson Microwave Anisotropy Probe* (*WMAP*; Bennett et al. 2013) as described in Section 4.1, which provide an excellent description of all our measurements.

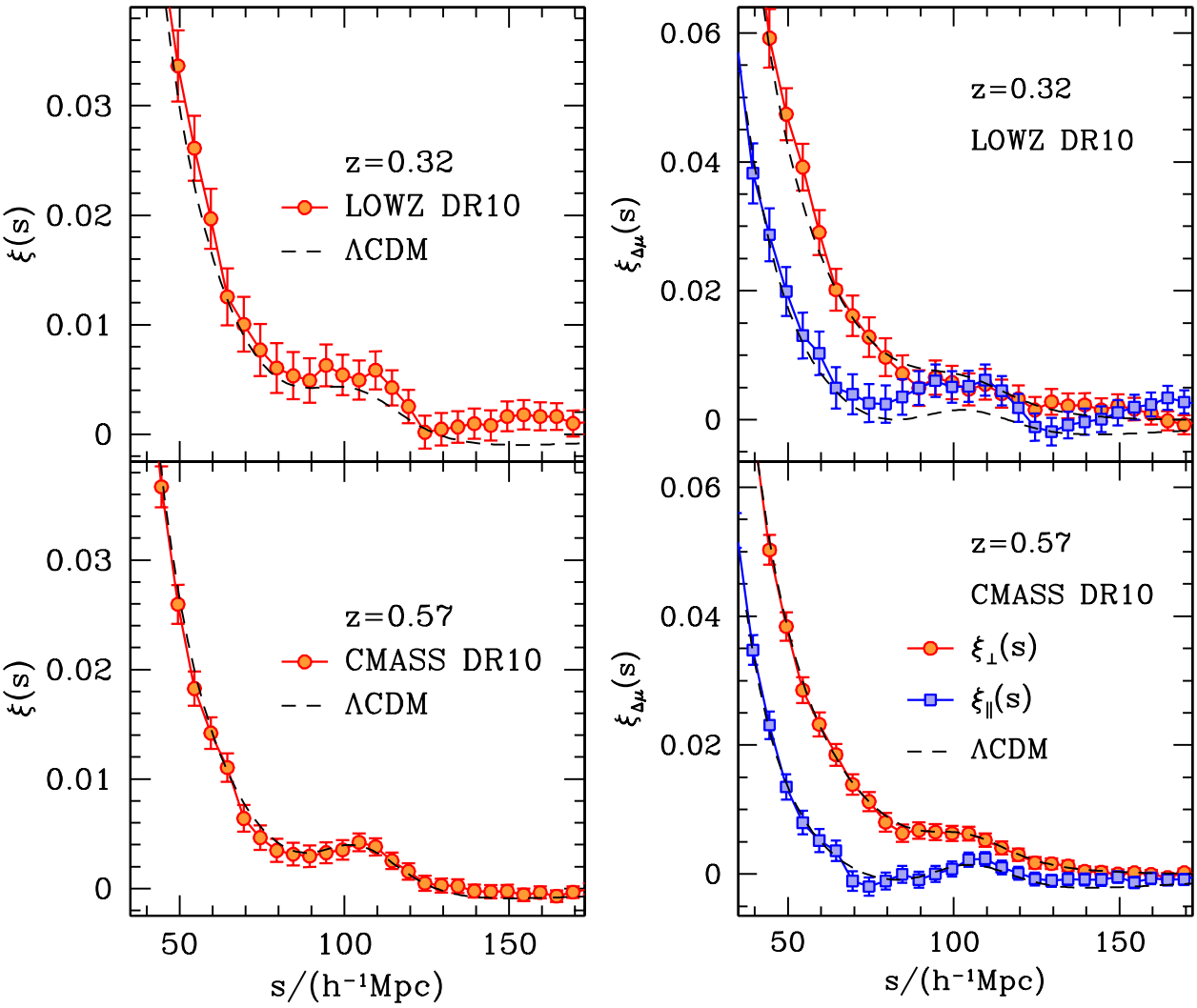

Figure 1. Angle-averaged correlation functions $\xi(s)$ (left-hand panels) and clustering wedges $\xi_\perp(s)$ and $\xi_\parallel(s)$ (right-hand panels) of the LOWZ and CMASS DR10 galaxy samples. The error bars were derived from the diagonal entries of the full covariance matrices obtained as described in Section 2.1.2. The dashed lines correspond to the best-fitting ΛCDM model obtained from the combination of information from the full shape of the LOWZ and CMASS DR11 clustering wedges with the CMB temperature fluctuation measurements from *Planck* and the 9 yr polarization measurements from *WMAP* (see Section 4.1).

2.1.2 *Covariance matrix estimation*

When comparing our BOSS clustering measurements with theoretical predictions, we assume a Gaussian likelihood function of the form $\mathcal{L} \propto \exp(-\chi^2/2)$. The calculation of the χ^2 value of a given model requires the knowledge of the inverse covariance matrix of our measurements, which we estimate using mock catalogues matching the selection functions of the LOWZ and CMASS samples. These mocks were constructed from two sets of PTHALOS realizations (Scoccimarro & Sheth 2002), corresponding to our fiducial cosmology, as described in Manera et al. (2013, 2014).[1] Our CMASS mocks are based on 600 independent simulations with a box size of $L_{\rm box} = 2.4\,h^{-1}$ Gpc, while those of the LOWZ sample were constructed from a separate set of 500 boxes with the same volume. In the construction of these mocks, the Northern Galactic Cap (NGC) and Southern Galactic Cap (SGC) components of the survey were considered as being independent, and sampled separately from the same PTHALOS realizations. The volume of the LOWZ sample allowed us to obtain two separate NGC and SGC mocks per PTHALOS realization, leading to 1000 independent combined NGC+SGC LOWZ mock catalogues. The larger volume of the CMASS sample makes it more difficult to construct mocks of the NGC and SGC components from the boxes without overlap. This means that the NGC and SGC CMASS mocks drawn from the same box are not independent. For DR10, the overlap between the NGC and SGC mocks is approximately 75 per cent of the area covered by the SGC, while for DR11 the whole of the Southern component is also covered by the NGC. To account for this overlap in our covariance matrix estimations, we construct two sets of 300 independent NGC+SGC CMASS mocks, drawing the matched components from different boxes.

We measured the angle-averaged correlation function and the clustering wedges of each LOWZ and CMASS mock catalogue using the same binning and weighting schemes as for the real data. These measurements were used to obtain an estimate of the full covariance matrix **C** of our clustering measurements. For the CMASS sample, we define our covariance matrix as the average of the results

[1] http://www.marcmanera.net/mocks/

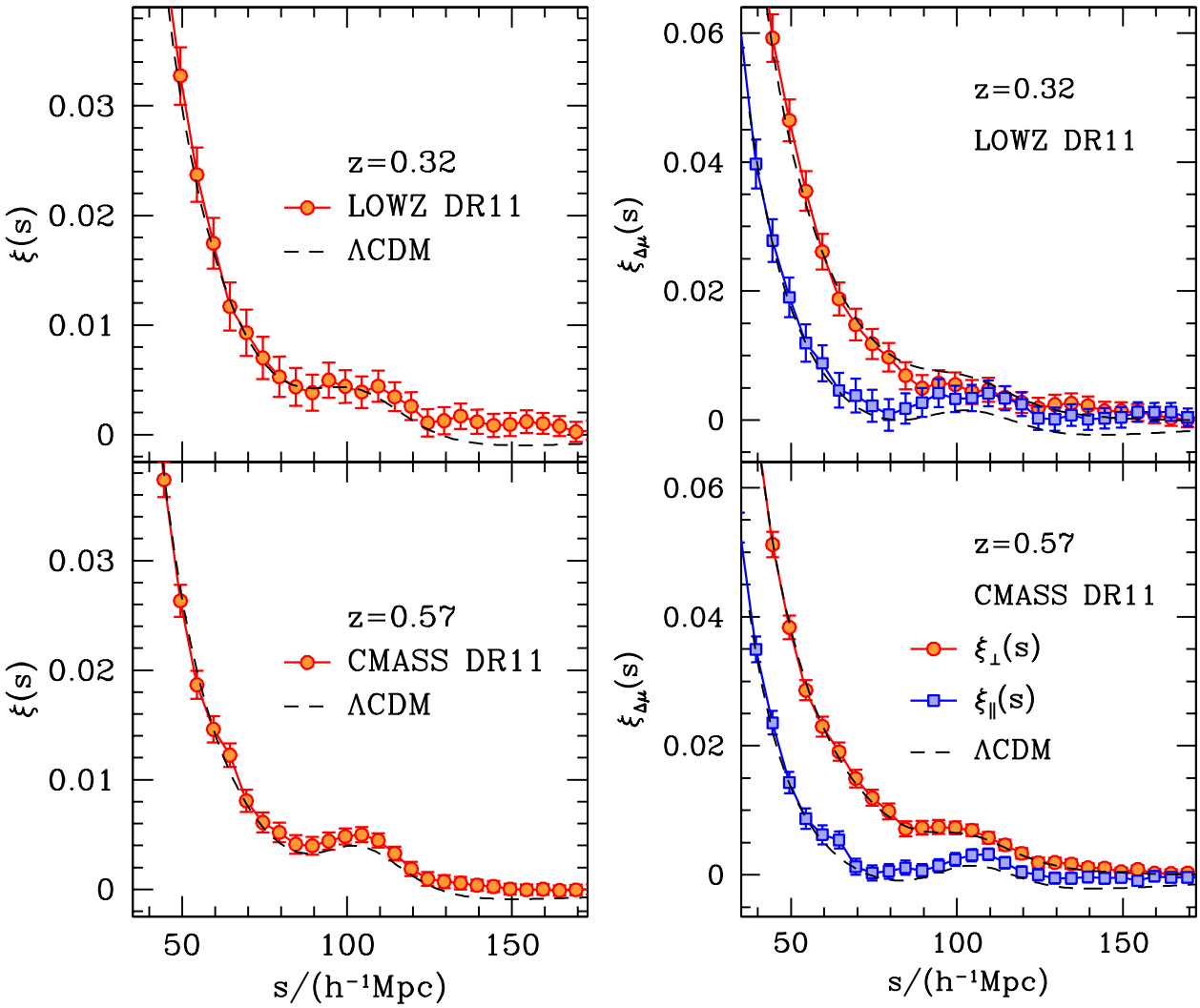

Figure 2. The same as Fig. 1, but for the LOWZ and CMASS DR11 galaxy samples.

obtained in the two sets of independent mocks. The error bars in Figs 1 and 2 correspond to the square root of the diagonal entries in $\mathbf{C}$.

Our estimations of $\mathbf{C}$ are affected by noise, as they are inferred from a finite number of mock catalogues. This uncertainty has important implications on the derived constraints. The distribution of covariance matrices recovered from multiple, independent sets of simulations follows a Wishart distribution, and its inverse, $\mathbf{C}^{-1}$, an inverse Wishart distribution (Wishart 1928). As the inverse Wishart distribution is asymmetric, $\mathbf{C}^{-1}$ provides a biased estimate of the true inverse covariance matrix (see e.g. Hartlap, Simon & Schneider 2007; Percival et al. 2014; Taylor, Joachimi & Kitching 2013). This bias can be corrected for by rescaling the inverse covariance matrix as

$$\hat{\mathbf{C}}^{-1} = (1 - D)\,\mathbf{C}^{-1}, \tag{3}$$

with

$$D = \frac{N_{\rm bins} + 1}{N_{\rm mocks} - 1}, \tag{4}$$

where $N_{\rm mocks}$ is to the total number of mocks used to estimate $\mathbf{C}$ and $N_{\rm bins}$ corresponds to the total number of bins in our measurements. We restrict our analysis to $40 < s < 160\,h^{-1}$ Mpc with a bin width of $\mathrm{d}s = 5\,h^{-1}$ Mpc, leading to $N_{\rm bins} = 30$ for the angle-averaged correlation function and $N_{\rm bins} = 60$ for the clustering wedges.

Equation (4) shows that an accurate estimate of the inverse covariance matrix requires a large number of independent realizations. While for the LOWZ sample our covariance matrix estimates are based on $N_{\rm mocks} = 1000$, for the CMASS sample we use two sets of 300 independent mocks. As these two sets are correlated, their combination does not lead to the same noise that would correspond to using 600 independent estimates. To account for this fact, we follow Percival et al. (2014) and compute the correction term D in equation (4) using $N_{\rm mocks} = 300$, and multiply the result by $(1 + r^2)/2$, where r corresponds to the correlation coefficient between the mock clustering measurements. The volume overlap between our mock catalogues implies $r = 0.33$ for DR10 and $r = 0.49$ for DR11 (for more details, see Percival et al. 2014). The resulting correction factors for the clustering measurements used in our analysis are listed in Table 1.

Although the correction factor of equation (4) leads to an unbiased estimation of the inverse covariance matrix, it does not correct for the effect of the uncertainties in this estimate, which should be propagated into the obtained cosmological constraints. Percival et al. (2014) present a detailed description of the effect of the noise in the covariance matrix estimated from a set of mock realizations and

Table 1. Correction factors of equation (4) to account for the bias in the estimation of the inverse covariance matrix.

Measurement	$(1-D)$
DR10 and DR11 LOWZ $\xi(s)$	0.978
DR10 and DR11 LOWZ $\xi_{\Delta\mu}(s)$	0.953
DR10 CMASS $\xi(s)$	0.955
DR10 CMASS $\xi_{\Delta\mu}(s)$	0.913
DR11 CMASS $\xi(s)$	0.950
DR11 CMASS $\xi_{\Delta\mu}(s)$	0.902

derive formulae for their impact on the errors of the cosmological constraints measured by integrating over the likelihood function. They demonstrated that, to account for this extra uncertainty, the recovered parameter constraints must be rescaled by a factor that depends on $N_{\rm bins}$, $N_{\rm mocks}$ and the number of parameters included in the analysis, $N_{\rm par}$ (see equation 18 in Percival et al. 2014). Depending on the parameter space, our choice of range of scales and binning leads to a modest correction factor of at most 2.4 per cent for the results inferred from the clustering wedges, which we include in our constraints, and a negligible correction (less than 0.3 per cent) for the results obtained from the angle-averaged correlation function.

2.2 Additional data sets

We combine the information encoded in the full shape of our clustering measurements with additional observations in order to improve the obtained cosmological constraints. Here we give a brief description of each additional data set.

We use the low-ℓ and high-ℓ CMB temperature power spectrum from the 1 yr data release of the *Planck* satellite (Planck Collaboration I 2013) with the low-ℓ polarization measurements from the 9 yr of observations of the *WMAP* satellite (Bennett et al. 2013; Hinshaw et al. 2013). This data set corresponds to the '*Planck*+WP' case considered in Planck Collaboration XVI (2013). For simplicity, we refer to this combination simply as '*Planck*'. We extend this data set using the high-ℓ CMB measurements from the Atacama Cosmology Telescope (ACT; Das et al. 2013) and the South Pole Telescope (SPT; Keisler et al. 2011; Reichardt et al. 2012; Story et al. 2013). We refer to this combination as 'ePlanck'. We also explore the constraints obtained by replacing the *Planck* CMB data by the final 9 yr results from the *WMAP* satellite (Bennett et al. 2013; Hinshaw et al. 2013) to test the consistency between these data sets. We refer to these measurements as '*WMAP*9'.

We also include information from distance measurements inferred from the angle-averaged BAO signal from independent samples. We use the results of Beutler et al. (2011) from the large-scale correlation function of the 6dF Galaxy Survey (Jones et al. 2009) corresponding to $z = 0.106$, and the distance measurements inferred from the Lyman α forest in BOSS (Busca et al. 2013; Kirkby et al. 2013; Slosar et al. 2013), corresponding to $z = 2.4$. These data sets constrain the parameter combination $D_{\rm V}(z)/r_{\rm d}$, where

$$D_{\rm V}(z) = \left((1+z)^2 D_{\rm A}(z)^2 \frac{cz}{H(z)}\right)^{1/3}. \quad (5)$$

We do not include the results of Xu et al. (2012) based on the final SDSS-II LRG sample as this catalogue is partially contained in the LOWZ sample used here or the results from Blake et al. (2011) from the final WiggleZ Dark Energy Survey (Drinkwater et al. 2010) at $z = 0.44$, 0.6 and 0.73 due to the overlap of these data with the CMASS sample.

Finally, we also use the information from the Union2.1 Type Ia supernova (SN) compilation (Suzuki et al. 2012). This sample combines 833 SN drawn from 19 different data sets using the scheme of the original Union sample of Kowalski et al. (2008). For comparison, in some cases we also present results obtained using the SN compilation of Conley et al. (2011), which includes the high-redshift SN from the first three years of the Supernova Legacy Survey (SNLS). When using these data, we follow the recipe of Conley et al. (2011) to take into account systematic errors in our cosmological constraints, which requires the introduction of two additional nuisance parameters, α and β, related to the stretch–luminosity and colour–luminosity relationships. When quoting cosmological constraints based on this sample, the values of these parameters are marginalized over.

With the exception of Section 3.3, we use our BOSS clustering measurements in combination with CMB data. Unless stated otherwise, we use the information from our clustering measurements in the LOWZ and CMASS samples in combination, and refer to them as 'BOSS $\xi(s)$' for the angle-averaged correlation functions and 'BOSS $\xi_{\Delta\mu}(s)$' for the clustering wedges. Although the bulk of our analysis is based on our DR11 BOSS clustering measurements as they possess smaller statistical uncertainties, we test the consistency of these results with the constraints inferred using their DR10 counterparts. Our tightest constraints are obtained when the additional BAO and Union2.1 SN data are also included in our analysis. We refer to this case as our 'Full' combination.

3 METHODOLOGY

3.1 Modelling of our clustering measurements

We follow the recipe of Sánchez et al. (2013) to model the full shape of the angle-averaged correlation function and the clustering wedges. This description takes into account the effects of non-linear evolution, RSD and bias which, if unaccounted for, could introduce systematic errors in the derived cosmological constraints (Angulo et al. 2008; Crocce & Scoccimarro 2008; Sánchez, Baugh & Angulo 2008; Smith, Scoccimarro & Sheth 2008). Here we summarize the main details of our modelling and refer the reader to section 3 of Sánchez et al. (2013) for more details.

Both the angle-averaged correlation function and the clustering wedges can be obtained by integrating $\xi(\mu, s)$ over different μ intervals. This means that a theoretical description of these measurements requires a model of the anisotropic correlation function. To obtain this model, it is convenient to decompose $\xi(\mu, s)$ in terms of Legendre polynomials, $L_\ell(\mu)$, as

$$\xi(\mu, s) = \sum_{\rm even\ \ell} L_\ell(\mu)\xi_\ell(s), \quad (6)$$

where the multipoles $\xi_\ell(s)$ are given by

$$\xi_\ell(s) \equiv \frac{2\ell+1}{2}\int_{-1}^{1} L_\ell(\mu)\xi(\mu, s)\,{\rm d}\mu. \quad (7)$$

These multipoles are related to those of the two-dimensional power spectrum, $P(\mu, k)$, by

$$\xi_\ell(s) \equiv \frac{i^\ell}{2\pi^2}\int_0^\infty P_\ell(k) j_\ell(ks)\, k^2 {\rm d}k, \quad (8)$$

where $j_\ell(x)$ is the spherical Bessel function of order ℓ (Hamilton 1997). We describe $P(\mu, k)$ with a simple parametrization as

$$P(\mu, k) = \left(\frac{1}{1+(kf\sigma_{\rm v}\mu)^2}\right)^2 (1+\beta\mu^2)^2 P_{\rm NL}(k), \quad (9)$$

where $f \equiv \frac{\mathrm{d}\ln D}{\mathrm{d}\ln a}$ is the logarithmic structure growth-rate parameter, $\beta = f/b$, and $P_{\rm NL}(k)$ represents the non-linear real-space power spectrum, given by

$$P_{\rm NL}(k) = b^2 \left[P_{\rm L}(k)\, \mathrm{e}^{-(k\sigma_{\rm v})^2} + A_{\rm MC}\, P_{\rm MC}(k) \right] \tag{10}$$

with b, $\sigma_{\rm v}$ and $A_{\rm MC}$ treated as free parameters. Here $P_{\rm MC}(k)$ is given by

$$P_{\rm MC}(k) = \frac{1}{4\pi^3} \int \mathrm{d}^3 q\, |F_2(\boldsymbol{k}-\boldsymbol{q}, \boldsymbol{q})|^2 P(|\boldsymbol{k}-\boldsymbol{q}|) P(q), \tag{11}$$

where $F_2(\boldsymbol{k}, \boldsymbol{q})$ is the standard second-order kernel of perturbation theory. The parametrization of equation (10) is motivated by renormalized perturbation theory (RPT; Crocce & Scoccimarro 2006) and is the basis of the parametrization of the non-linear correlation function proposed by Crocce & Scoccimarro (2008). This simple recipe provides an accurate description of the power spectra and correlation functions measured from N-body simulations (e.g. Sánchez et al. 2008; Montesano, Sánchez & Phleps 2010) and has been applied to the analysis of numerous galaxy samples (Sánchez et al. 2009, 2012, 2013; Beutler et al. 2011; Blake et al. 2011; Montesano, Sánchez & Phleps 2012). The Lorentzian pre-factor in equation (9) accounts for the Finger-of-God effect (Jackson 1972) under the assumption of an exponential galaxy velocity distribution function (Park et al. 1994; Cole, Fisher & Weinberg 1995).

Only a small number of multipoles of $\xi(\mu, s)$ have non-negligible values on large scales. We base our description of the full $\xi(\mu, s)$ on the multipoles $\xi_\ell(s)$ with $\ell = 0$, 2 of the parametrization of equation (9). Sánchez et al. (2013) showed that discarding contributions from multipoles with $\ell \geq 4$, this simple recipe provides an accurate description of the full shape of the angle-averaged correlation function and the clustering wedges $\xi_\perp(s)$ and $\xi_\parallel(s)$, leading to unbiased cosmological constraints.

One additional ingredient must be added to our model before it can be compared with real clustering measurements. As described in Section 2.1.1, these measurements require the assumption of a fiducial cosmology to convert the observed redshifts into distances. This choice must be taken into account in our models. The relation between the true values of s and μ characterizing a given galaxy pair and those measured assuming a different fiducial cosmology can be written as (Ballinger, Peacock & Heavens 1996)

$$s = s' \sqrt{\alpha_\parallel^2 (\mu')^2 + \alpha_\perp^2 (1-(\mu')^2)}, \tag{12}$$

$$\mu = \frac{\alpha_\parallel \mu'}{\sqrt{\alpha_\parallel^2 (\mu')^2 + \alpha_\perp^2 (1-(\mu')^2)}}, \tag{13}$$

where the primes denote the quantities in the fiducial cosmology and the scaling factors are given by

$$\alpha_\perp = \frac{D_{\rm A}(z_{\rm m})}{D'_{\rm A}(z_{\rm m})}, \tag{14}$$

$$\alpha_\parallel = \frac{H'(z_{\rm m})}{H(z_{\rm m})}, \tag{15}$$

that is, the ratios of the angular diameter distance and the Hubble parameter evaluated at the mean redshift of the sample being considered, $z_{\rm m}$. These relations encode the effect of the fiducial cosmology on our clustering measurements, as they can be used to transform the integral in equation (1) from the fiducial cosmology space to the true cosmology as

$$\xi'_{\Delta\mu}(s') \equiv \frac{1}{\Delta\mu'} \int_{\mu'_{\rm min}}^{\mu'_{\rm max}} \xi(\mu(\mu', s'), s(\mu', s'))\, \mathrm{d}\mu'. \tag{16}$$

We use this relation to transform our theoretical predictions of $\xi(s)$ and $\xi_{\Delta\mu}(s)$ to the fiducial cosmology assumed in our BOSS clustering measurements.

3.2 Cosmological parameter spaces

We assume that primordial fluctuations are adiabatic, Gaussian and have a power-law spectrum of Fourier amplitudes, with a negligible tensor component. Table 2 lists the parameters that specify a given cosmological model under these assumptions. We use the data sets described in Section 2 to obtain constraints on these parameters. We start our analysis with the basic ΛCDM parameter space, which corresponds to a flat universe where the energy budget contains contributions from baryons, CDM and dark energy, described by an equation of state $w_{\rm DE} = p_{\rm DE}/\rho_{\rm DE} = -1$. We follow Planck Collaboration XVI (2013) and assume a non-zero fraction of massive neutrinos with a fixed total mass $\sum m_\nu = 0.06$ eV. The free parameters required to characterize this model are listed in the upper part of Table 2. Although it is considered in our analysis, the optical depth to reionization, τ, is constrained by the CMB data alone and including additional data sets leaves the results unchanged. As Hinshaw et al. (2013) and Planck Collaboration XVI (2013) present constraints

Table 2. Cosmological parameters considered in our analysis. The upper part lists the parameters of the standard ΛCDM model while the middle section lists a number of possible extensions of this parameter space. The lower part lists a number of important quantities whose values can be derived from the first two sets.

Parameter	Description
Basic ΛCDM parameters	
$\theta_{\rm MC}$	Approximate angular size of the sound horizon at recombination[a]
$\omega_{\rm b}$	Physical baryon density
$\omega_{\rm c}$	Physical CDM density
τ	Optical depth to reionization
$n_{\rm s}$	Scalar spectral index[b]
$A_{\rm s}$	Amplitude of the scalar perturbations[b]
Additional parameters	
Ω_k	Curvature contribution to energy density
w_0	Present-day dark energy equation of state, $w_{\rm DE}$
w_a	Time dependence of $w_{\rm DE}$ (assuming $w_{\rm DE}(a) = w_0 + w_a(1-a)$)
$\sum m_\nu$	Total sum of the neutrino masses
$N_{\rm eff}$	Effective number of relativistic species
γ	Power-law index of the structure growth-rate parameter, assuming $f(z) = \Omega_{\rm m}^\gamma$
Derived parameters	
$\Omega_{\rm m}$	Total matter density
$\Omega_{\rm DE}$	Dark energy density
h	Dimensionless Hubble parameter
t_0/Gyr	Age of the Universe
σ_8	Linear-theory rms mass fluctuations in spheres of radius $8\,h^{-1}$ Mpc
f_ν	Dark matter fraction in massive neutrinos
$f(z_{\rm m})$	Structure growth-rate parameter, $f(z) = \frac{d\ln D}{d\ln a}$

[a]Defined as in the June 2013 version of COSMOMC.
[b]Quoted at the pivot wavenumber of $k_0 = 0.05\,\mathrm{Mpc}^{-1}$.

on this parameter based on the same CMB measurements used in our analysis, we do not report them here.

We also explore a number of possible extensions of the ΛCDM parameter space by allowing for variations on the additional parameters presented in the middle section of Table 2. These extensions include more general dark energy models, non-flat universes, different contributions from massive neutrinos, additional relativistic species and possible deviations from the predictions of general relativity (GR). The final part of Table 2 lists a number of important quantities whose values can be derived from the remaining parameters.

When studying the properties of the dark energy component, we explore the cases of a time-independent dark energy equation of state $w_{\rm DE}$ and when this parameter is allowed to vary with time, in which case we assume the standard parametrization of Chevallier & Polarski (2001) and Linder (2003) given by

$$w_{\rm DE}(a) = w_0 + w_a(1-a). \quad (17)$$

When exploring the constraints on other potential extensions of the ΛCDM model, we investigate the impact of allowing also for variations on $w_{\rm DE}$.

We explore these parameter spaces by means of the Markov chain Monte Carlo (MCMC) technique. We use the June 2013 version of COSMOMC (Lewis & Bridle 2002), modified to include our BOSS clustering measurements as additional data sets. This code uses CAMB to compute power spectra for the CMB and matter fluctuations (Lewis, Challinor & Lasenby 2000), which implements the parametrized post-Friedman framework (Hu & Sawicki 2007) to account for models with $w_{\rm DE} < -1$ and dynamical dark energy models, as described in Fang, Hu & Lewis (2008). Besides the cosmological parameters described here, the analysis of the CMB data requires the inclusion of a number of nuisance parameters that are included in our MCMC and marginalized over, as described in Planck Collaboration XVI (2013). When including clustering measurements from BOSS in our analysis, the parameters b, $\sigma_{\rm v}$ and $A_{\rm MC}$ for each data set are included as additional free parameters in our MCMC and marginalized over.

3.3 The cosmological information in the correlation function and the clustering wedges

In this section, we analyse the information on geometrical quantities encoded in our measurements of $\xi(s)$ and the clustering wedges $\xi_\perp(s)$ and $\xi_\parallel(s)$. As discussed in detail by Kazin et al. (2012), while angle-averaged measurements such as $\xi(s)$ provide constraints on the ratio $D_{\rm V}(z_{\rm m})/r_{\rm d}$, anisotropic clustering measurements such as the clustering wedges constrain the combinations $D_{\rm A}(z_{\rm m})/r_{\rm d}$ and $H(z_{\rm m})r_{\rm d}$. In this way, the BAO signal in the clustering wedges can be used to break the degeneracy between $D_{\rm A}(z_{\rm m})$ and $H(z_{\rm m})$ obtained from $\xi(s)$. When the full shape of these measurements is taken into account, the extra information on $f(z_{\rm m})$ provided by the amplitude difference between $\xi_\perp(s)$ and $\xi_\parallel(s)$ improves the constraints from those recovered when only the BAO signal is considered (Sánchez et al. 2013).

We now investigate the constraints on these quantities that can be derived from our clustering measurements. To do this, we explore our most general parameter space treating these quantities as derived parameters, with their values computed in the context of the cosmological model being tested. This approach differs from the one applied in our companion papers (Beutler et al. 2013; Chuang et al. 2013b; Samushia et al. 2014; Anderson et al. 2013; Tojeiro et al. 2014) where the values of $D_{\rm A}(z)$ and $H(z)$ are treated as independent parameters (i.e. without adopting a specific relation between their values). While the approach followed in these analyses will lead to more general constraints on these parameters than the ones derived here, our results can be used as an indication of the information content in our clustering measurements and a consistency test with the results of these analyses. For this exercise, we apply flat priors on the parameters $\Phi = (\omega_{\rm b}, \omega_{\rm c}, n_{\rm s})$, which determine the shape of the linear-theory matter power spectrum, centred on the values corresponding to the best-fitting ΛCDM model to the *Planck* CMB data, with a width equivalent to six times their 68 per cent confidence levels (CL).

Table 3. Marginalized 68 per cent geometrical constraints derived from the full shape of our clustering measurements alone, under the assumption that $f(z_{\rm m})$ follows the predictions of GR. We have rescaled our results by the sound horizon at the drag redshift for our fiducial cosmology, $r_{\rm d}^{\rm fid} = 149.28$ Mpc, to express them in units of Mpc and km s^{-1} Mpc^{-1}.

Data set	$D_{\rm V}(z)\left(\frac{r_{\rm d}^{\rm fid}}{r_{\rm d}}\right)$	$D_{\rm A}(z)\left(\frac{r_{\rm d}^{\rm fid}}{r_{\rm d}}\right)$	$H(z)\left(\frac{r_{\rm d}}{r_{\rm d}^{\rm fid}}\right)$
CMASS ($z_{\rm m} = 0.57$)			
DR11 $\xi(s)$	2054 ± 25	–	–
DR11 $\xi_{\Delta\mu}(s)$	2048 ± 25	1387 ± 22	94.3 ± 2.4
DR10 $\xi(s)$	2046 ± 34	–	–
DR10 $\xi_{\Delta\mu}(s)$	2034 ± 31	1385 ± 28	96.0 ± 3.4
LOWZ ($z_{\rm m} = 0.32$)			
DR11 $\xi(s)$	1254 ± 56	–	–
DR11 $\xi_{\Delta\mu}(s)$	1237 ± 42	965 ± 37	82.5 ± 3.5
DR10 $\xi(s)$	1266 ± 48	–	–
DR10 $\xi_{\Delta\mu}(s)$	1237 ± 42	960 ± 34	81.6 ± 3.9

Table 3 lists the geometrical constraints obtained from the full shape of our clustering measurements alone, assuming that $f(z_{\rm m})$ follows the predictions of GR. Here we have rescaled our results by the sound horizon at the drag redshift for our fiducial cosmology computed using CAMB, $r_{\rm d}^{\rm fid} = 149.28$ Mpc, to express them in units of Mpc and km s^{-1} Mpc^{-1}. In all cases, the results recovered from the DR10 and DR11 samples are in good agreement. For the CMASS sample, the extra volume of DR11 leads to a reduction of approximately 20 per cent in the allowed regions. For the DR11 LOWZ sample, although the limits on $H(z_{\rm m})$ and $D_{\rm A}(z_{\rm m})$ inferred from the clustering wedges exhibit an improvement of about 10 per cent with respect to the corresponding DR10 results, the constraints on $D_{\rm V}(z_{\rm m})$ obtained from $\xi(s)$ show the opposite behaviour. This is consistent with the results of the BAO-only analysis of Tojeiro et al. (2014) and might be related to the higher amplitude of the acoustic peak in the DR10 LOWZ $\xi(s)$, which leads to a more accurate determination of its centroid. Fig. 3 shows the two-dimensional marginalized constraints on $D_{\rm A}(z_{\rm m})(r_{\rm d}^{\rm fid}/r_{\rm d})$ and $H(z_{\rm m})(r_{\rm d}/r_{\rm d}^{\rm fid})$ at $z_{\rm m} = 0.32$ (left-hand panel) and $z_{\rm m} = 0.57$ (right-hand panel), derived from the DR11 LOWZ and CMASS samples, respectively. The long-dashed lines correspond to the constraints derived from the angle-averaged correlation function, which correspond to a degeneracy of constant $D_{\rm V}(z_{\rm m})/r_{\rm d}$. For each sample, the extra information contained in the clustering wedges breaks this degeneracy, leading to separate constraints on $D_{\rm A}$ and H shown by the solid lines.

We also test the effect of relaxing the assumption of GR to compute $f(z_{\rm m})$ by treating its value as a free parameter. Table 4 summarizes the results obtained from the clustering wedges of our galaxy samples, which are in good agreement with the ones obtained from the BAO-only analysis of the same galaxy samples in Anderson et al. (2013) and Tojeiro et al. (2014). Exploring this parameter

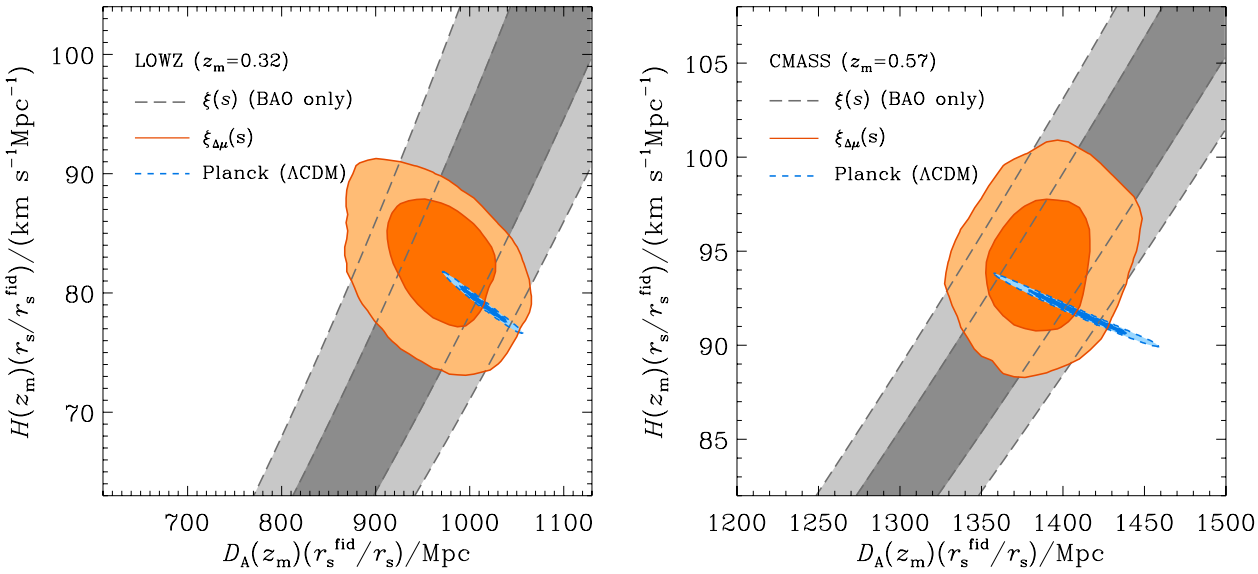

Figure 3. Two-dimensional marginalized constraints in the $D_A(z_m)(r_d^{fid}/r_d)-H(z_m)(r_d/r_d^{fid})$ plane at $z_m = 0.32$ (left-hand panel) and $z_m = 0.57$ (right-hand panel) derived from the LOWZ and CMASS DR11 samples, respectively. The grey long-dashed contours show the results obtained using information from the angle-averaged correlation function while the red solid lines correspond to those inferred from the clustering wedges $\xi_\perp(s)$ and $\xi_\parallel(s)$ assuming that $f(z)$ follows the predictions of GR. The short-dashed contours correspond to the prediction for these parameters derived from the ePlanck data set (see Section 2.2) under the assumption of a ΛCDM model.

Table 4. Marginalized 68 per cent constraints on geometrical quantities and the growth of structure derived from the full shape of our clustering wedges, when the assumption that $f(z_m)$ follows the predictions of GR is relaxed. We have rescaled our results by the sound horizon at the drag redshift for our fiducial cosmology, $r_d^{fid} = 149.28$ Mpc, to express them in units of Mpc and km s^{-1} Mpc^{-1}.

Data set	$D_A(z)\left(\frac{r_d^{fid}}{r_d}\right)$	$H(z)\left(\frac{r_d}{r_d^{fid}}\right)$	$f(z)\sigma_8(z)$
CMASS ($z_m = 0.57$)			
DR11 $\xi_{\Delta\mu}(s)$	1382 ± 26	93.5 ± 3.0	0.417 ± 0.045
DR10 $\xi_{\Delta\mu}(s)$	1381 ± 31	$95.5^{+3.7}_{-3.2}$	0.469 ± 0.060
LOWZ ($z_m = 0.32$)			
DR11 $\xi_{\Delta\mu}(s)$	965 ± 42	$81.7^{+4.0}_{-4.4}$	0.48 ± 0.10
DR10 $\xi_{\Delta\mu}(s)$	951 ± 39	80.4 ± 3.2	0.43 ± 0.10

space we can constrain the combination $f\sigma_8(z)$, for which we obtain $f\sigma_8(0.32) = 0.48 \pm 0.10$ and $f\sigma_8(0.57) = 0.417 \pm 0.045$ using the information of the DR11 LOWZ and CMASS galaxy samples, respectively. The constraint derived from the DR11 CMASS sample is in excellent agreement with the results of Beutler et al. (2013) and Samushia et al. (2014), who found $f\sigma_8(0.57) = 0.419 \pm 0.042$ and $f\sigma_8(0.57) = 0.441 \pm 0.044$, respectively. Chuang et al. (2013b) use the information from the multipoles of the LOWZ and CMASS correlation functions for scales $56 \leq s/(h^{-1}\,\mathrm{Mpc}) \leq 200$ and find $f\sigma_8(0.32) = 0.384 \pm 0.095$ and $f\sigma_8(0.57) = 0.354 \pm 0.059$. Although these values are lower than the ones reported here, Chuang et al. (2013b) apply a significantly wider prior on the parameters Φ and find evidence for an increase in the recovered value for this quantity when smaller scales are included in the analysis.

The dashed lines in Fig. 3 correspond to the constraints obtained from the ePlanck CMB measurements under the assumption of a ΛCDM model. The results obtained from the clustering wedges are in good agreement with the predictions of the ΛCDM model that best describes these CMB data, indicating the consistency between these data sets and their agreement with the ΛCDM model. For more general parameter spaces, the region in the $D_A(z_m)(r_d^{fid}/r_d) - H(z_m)(r_d/r_d^{fid})$ plane allowed by the CMB data increases substantially. In these cases, the combination of the CMB data with the information provided by our clustering measurements improves the constraints over those recovered from the CMB information alone. In Section 4, we explore the cosmological implications of the information contained in our clustering measurements.

4 COSMOLOGICAL CONSTRAINTS

Here we describe the cosmological implications of our BOSS clustering measurements. Section 4.1 presents the constraints on the parameters of the standard ΛCDM model, while Sections 4.2–4.5 explore the results obtained in more general parameter spaces. We pay particular attention to the constraints on the properties of the dark energy component and study how the limits in other parameters are changed when more general dark energy models are considered. Appendix A gives a complete list of the cosmological constraints derived from different data set combinations, while Table 5 summarizes the results on the most important parameters for the various cases we consider.

4.1 The ΛCDM parameter space

The simple ΛCDM model is able to describe an ever increasing amount of precise cosmological observations, with the CMB measurements from the *Planck* satellite being perhaps the most striking example (Planck Collaboration XVI 2013). However, as the statistical uncertainties of these measurements improve, the careful analysis of the consistency of the results derived from different data sets becomes crucial as it can be used to detect the presence of systematic errors. Here we review the constraints on the parameters of the ΛCDM model obtained by combining our BOSS clustering measurements with different data sets.

Table 5. Marginalized 68 per cent constraints on the most relevant cosmological parameters of the parameter spaces analysed in Sections 4.1–4.5, obtained using different combinations of the data sets described in Section 2.

	ePlanck+BOSS $\xi(s)$	ePlanck+BOSS $\xi_{\Delta\mu}(s)$	ePlanck + BOSS $\xi_{\Delta\mu}(s)$ +BAO+SN
The ΛCDM model			
h	$0.6824^{+0.0072}_{-0.0072}$	0.6863 ± 0.0075	0.6876 ± 0.0072
$100\Omega_{\rm m}$	$30.22^{+0.94}_{-0.96}$	$29.71^{+0.97}_{-0.96}$	29.53 ± 0.91
Constant dark energy equation of state			
$w_{\rm DE}$	$-1.31^{+0.21}_{-0.16}$	-1.051 ± 0.076	-1.024 ± 0.052
$100\Omega_{\rm m}$	$24.9^{+3.4}_{-2.6}$	28.8 ± 1.6	29.3 ± 1.1
Time-dependent dark energy equation of state			
w_0	$-1.29^{+0.48}_{-0.46}$	$-0.83^{+0.38}_{-0.34}$	-0.95 ± 0.14
w_a	$-0.0^{+1.0}_{-1.1}$	$-0.61^{+0.89}_{-0.96}$	-0.29 ± 0.47
$100\Omega_{\rm m}$	$25.2^{+5.7}_{-6.6}$	$30.9^{+4.1}_{-3.6}$	29.5 ± 1.3
Non-flat models			
$100\Omega_k$	0.07 ± 0.31	0.10 ± 0.29	0.15 ± 0.29
$100\Omega_{\rm m}$	30.18 ± 0.96	$29.60^{+0.99}_{-0.97}$	29.11 ± 0.91
Curvature and dark energy			
$w_{\rm DE}$	$-1.53^{+0.24}_{-0.28}$	-1.05 ± 0.11	$-1.009^{+0.062}_{-0.060}$
$100\Omega_k$	$-0.38^{+0.24}_{-0.28}$	0.02 ± 0.43	-0.14 ± 0.33
$100\Omega_{\rm m}$	$22.0^{+3.2}_{-4.9}$	28.9 ± 2.0	29.4 ± 1.2
Massive neutrinos			
$\sum m_\nu$	<0.23 eV (95% CL)	<0.24 eV (95% CL)	<0.23 eV (95% CL)
f_ν	<0.017 (95% CL)	<0.019 (95% CL)	<0.017 (95% CL)
Massive neutrinos and dark energy			
$\sum m_\nu$	<0.49 eV (95% CL)	<0.47 eV (95% CL)	<0.33 eV (95% CL)
$w_{\rm DE}$	$-1.49^{+0.24}_{-0.30}$	-1.13 ± 0.12	-1.046 ± 0.063
Additional relativistic degrees of freedom			
$N_{\rm eff}$	3.35 ± 0.27	3.31 ± 0.27	3.30 ± 0.27
$100\Omega_{\rm m}$	29.7 ± 1.0	29.2 ± 1.1	29.1 ± 1.0
Deviations from GR			
γ	–	0.69 ± 0.15	0.69 ± 0.15
$100\Omega_{\rm m}$	–	$29.76^{+0.93}_{-0.90}$	29.62 ± 0.89
Dark energy and modified gravity			
γ	–	0.88 ± 0.22	0.75 ± 0.17
$w_{\rm DE}$	–	-1.15 ± 0.11	-1.055 ± 0.057

The blue dashed lines in Fig. 4 correspond to the constraints in the $\Omega_{\rm m}-h$ plane derived from the *Planck* (upper panel) and *WMAP*9 (lower panel) CMB measurements. Both sets of constraints are elongated along the same degeneracy, which approximately corresponds to a constant value of $\Omega_{\rm m}h^3$ (Percival et al. 2002; Planck Collaboration XVI 2013), indicated by the dotted lines. Along this degeneracy, the constraints from *WMAP*9 extend towards lower values of $\Omega_{\rm m}$ and higher values of h than those derived from the *Planck* data. This behaviour leads to different, but consistent, marginalized constraints on these parameters. As shown by the red solid lines in Fig. 4, when these CMB measurements are combined with the information from the LOWZ and CMASS DR11 clustering wedges, the obtained constraints are significantly improved, leading to $\Omega_{\rm m} = 0.283 \pm 0.010$ and $h = 0.6947 \pm 0.0097$ for the *WMAP*9+BOSS $\xi_{\Delta\mu}(s)$ combination and $\Omega_{\rm m} = 0.2974 \pm 0.0098$ and $h = 0.6859 \pm 0.0076$ for the *Planck*+BOSS $\xi_{\Delta\mu}(s)$ data set. Although the differences in the constraints from *Planck* and *WMAP*9 are propagated to these results, our BOSS DR11 clustering measurements select the lowest values of $\Omega_{\rm m}$ allowed by *Planck*, leading to final constraints which are consistent within 1σ with those derived using *WMAP*9. As shown in Table 5, using the angle-averaged correlation function of the LOWZ and CMASS DR11 samples leads to similar constraints.

The dashed lines in Figs 1 and 2 correspond to the best-fitting ΛCDM model to the *Planck*+BOSS $\xi_{\Delta\mu}(s)$ combination. This model provides an excellent description of the broad-band shape and the location of the BAO peak in these measurements, with χ^2 values of 49.7 and 48.3 over 52 degrees of freedom for the DR11 LOWZ and CMASS clustering wedges, respectively. Despite the fact that this model was obtained by fitting the clustering wedges of the DR11 galaxy samples, it also provides an excellent description of all our clustering measurements, including our DR10 results. This illustrates the consistency between these data sets, which can also be

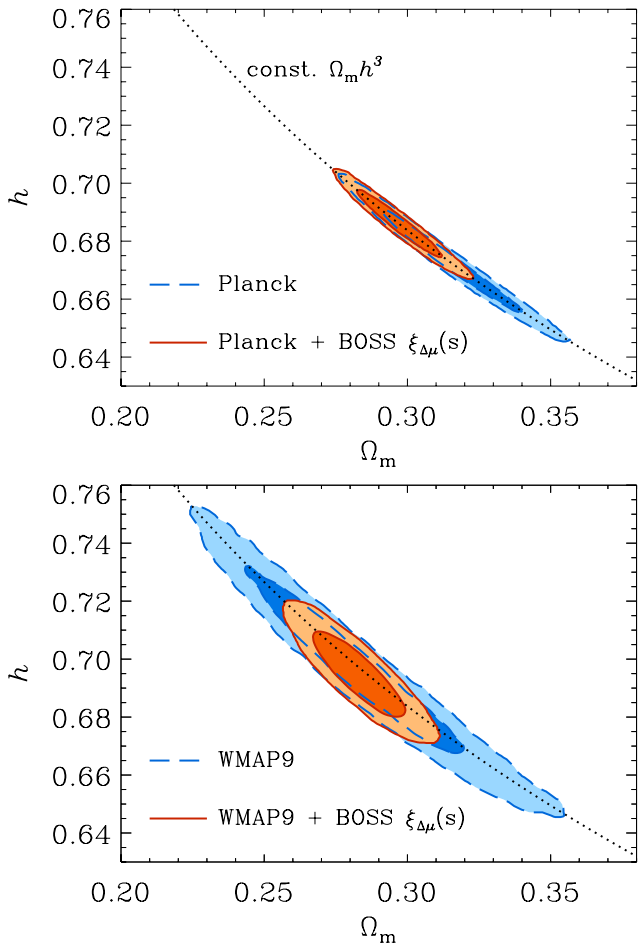

Figure 4. Two-dimensional marginalized constraints in the $\Omega_m - h$ plane. The blue dashed lines correspond to the constraints from the *Planck* (upper panel) and *WMAP*9 (lower panel) CMB measurements, which follow a degeneracy of constant $\Omega_m h^3 = 0.0959$, as indicated by the dotted lines. The red solid lines show the results obtained when these measurements are combined with the information from the LOWZ and CMASS DR11 clustering wedges.

seen in the cosmological constraints obtained when the *Planck* CMB data are combined with the DR10 LOWZ and CMASS clustering wedges, in which case we find $\Omega_m = 0.294 \pm 0.010$ and $h = 0.6882 \pm 0.0079$, in good agreement with the results obtained using DR11 information.

Our tightest constraints on the parameters of the ΛCDM model are obtained by combining the ePlanck CMB data set with the information from our DR11 BOSS $\xi_{\Delta\mu}(s)$, SN and BAO data sets, leading to $\Omega_m = 0.2924 \pm 0.0086$ and $h = 0.6899 \pm 0.0070$.

4.2 The dark energy equation of state

In the standard ΛCDM model, the current phase of accelerated cosmic expansion is due to a dark energy component characterized by a constant equation of state $w_{DE} = -1$. As this hypothesis is consistent with all current cosmological observations, it has become the standard model for dark energy. However, a variety of alternative models have been proposed (for a review, see e.g. Peebles & Ratra 2003; Frieman, Turner & Huterer 2008). Here we explore the constraints on more general dark energy models by allowing for variations in w_{DE} and its possible evolution with time.

We start our analysis by extending the ΛCDM parameter space including w_{DE}, assumed to be constant in time, as a free parameter. The blue long-dashed contours in Fig. 5 correspond to the 68 and 95 per cent CL in the $\Omega_m - w_{DE}$ plane obtained in this case from the *WMAP*9 (right-hand panel) and *Planck* (left-hand panel) CMB data. The constraints derived from both of these data sets exhibit a degeneracy between these parameters. However, the strong degeneracy seen in the *WMAP*9 constraints is somewhat reduced in the results derived from *Planck*, as the information from the higher acoustic peaks restricts the region of the parameter space with $w_{DE} > -1$. When these CMB data sets are combined with the information from the DR11 LOWZ and CMASS angle-averaged correlation functions, the allowed region for these parameters is reduced to a narrow degeneracy that is mostly driven by the D_V/r_d constraint provided by the CMASS sample (grey long-dashed lines in Fig. 5). In these cases, the dark energy equation of state is only weakly constrained, with $w_{DE} = -1.05^{+0.29}_{-0.13}$ and $w_{DE} = -1.28^{+0.24}_{-0.16}$ for the *WMAP*9+BOSS $\xi(s)$ and *Planck*+BOSS $\xi(s)$ combinations, respectively.

The red solid lines in Fig. 5 show the constraints obtained when the *WMAP*9 and *Planck* CMB data sets are combined with the information from the full shape of the DR11 LOWZ and CMASS clustering wedges. The additional information provided by $\xi_\perp(s)$ and $\xi_\parallel(s)$ can break the degeneracy present in the CMB results much more efficiently than the angle-averaged correlation function, leading to broadly similar results for both CMB data sets. In particular, the marginalized constraints on the matter density parameter are almost identical, with $\Omega_m = 0.288 \pm 0.015$ for the *WMAP*9+BOSS $\xi_{\Delta\mu}(s)$ case and $\Omega_m = 0.289 \pm 0.016$ for the *Planck*+BOSS $\xi_{\Delta\mu}(s)$ combination. However, the differences in the CMB data sets lead to slightly different constraints on the dark energy equation of state of $w_{DE} = -0.964 \pm 0.077$ (*WMAP*9+BOSS $\xi_{\Delta\mu}(s)$) and $w_{DE} = -1.049 \pm 0.078$ (*Planck*+BOSS $\xi_{\Delta\mu}(s)$). These results show that the combination of current CMB and LSS data sets can constrain the dark energy equation of state with an accuracy of 8 per cent, leading to results in good agreement with a cosmological constant, indicated by the dotted line in Fig. 5. Our results are consistent with those reported in our companion papers (Chuang et al. 2013b; Samushia et al. 2013a; Anderson et al. 2013), who find similar constraints on w_{DE} from the combination of CMB data with various types of anisotropic clustering information from the DR11 CMASS and LOWZ samples. This agreement illustrates the robustness of these limits with respect to the methodology implemented to obtain them.

Although the constraints obtained using the *WMAP*9 and *Planck* data sets are consistent at the 1σ level, the difference between these results highlights the importance of understanding the origin of the discrepancies between these data sets. The same behaviour is seen in other parameter spaces; once combined with our measurements of the LOWZ and CMASS clustering wedges, the *WMAP*9 and *Planck* CMB data sets give similar results, although the mean values are shifted by up to 1σ. In the following sections, we focus on the *Planck* CMB measurements and derive constraints using the ePlanck combination, but we compare the results with those derived using *WMAP*9 in some particular cases.

Combining the *Planck* CMB data with our DR10 clustering measurements leads to consistent results. The combination of *Planck* and the DR10 LOWZ and CMASS $\xi_{\Delta\mu}(s)$ provides the constraints $\Omega_m = 0.279 \pm 0.019$ and $w_{DE} = -1.092^{+0.092}_{-0.088}$. The smaller statistical uncertainties associated with the DR11 LOWZ and CMASS clustering measurements lead to a reduction of ∼15 per cent in the constraints on the dark energy equation of state. As the same

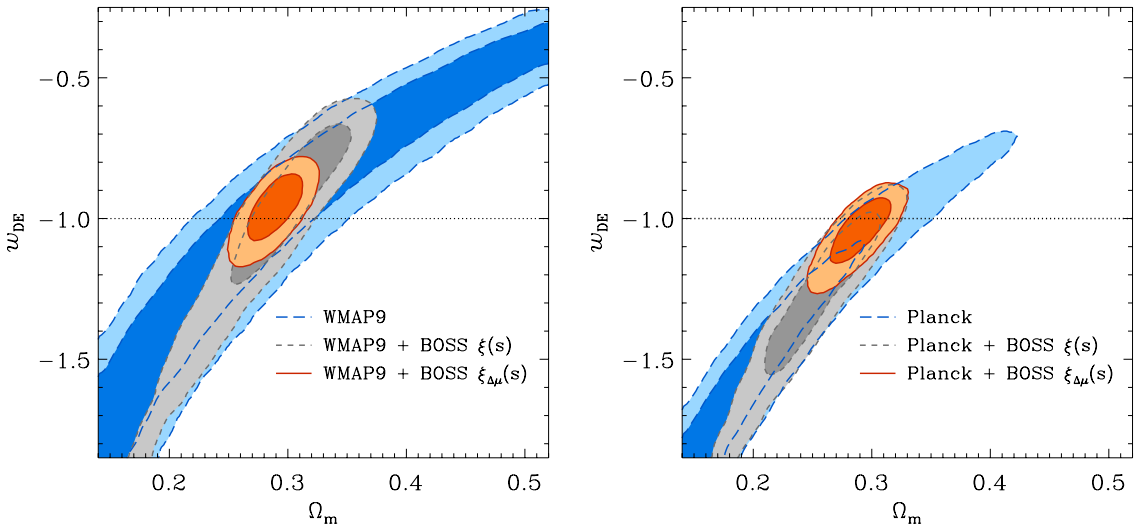

Figure 5. Left-hand panel: marginalized 68 and 95 per cent CL in the $\Omega_m - w_{DE}$ plane for the ΛCDM parameter set extended by including the redshift-independent value of w_{DE} as an additional parameter. The contours correspond to the results obtained using the *WMAP9*-only (blue long-dashed lines), the *WMAP9*+BOSS $\xi(s)$ combination (grey short-dashed lines) and the *WMAP9*+BOSS $\xi_{\Delta\mu}(s)$ case (red solid lines). The right-hand panel shows the results obtained when the *WMAP9* measurements are replaced by the *Planck* CMB data set. The dotted line in both panels corresponds to the ΛCDM model value of $w_{DE} = -1$.

agreement is seen in all cosmological parameter spaces, from now on we focus on the results obtained using the DR11 galaxy samples.

Including the information from the high-ℓ CMB experiments improves the constraints only marginally. Using the ePlanck + BOSS $\xi_{\Delta\mu}(s)$ combination, we find $w_{DE} = -1.051 \pm 0.076$. Our final constraints are obtained when the information from the additional BAO and Union2.1 SN measurements is added to this data combination, leading to $w_{DE} = -1.024 \pm 0.052$, in good agreement with the ΛCDM model value of $w_{DE} = -1$ and $\Omega_m = 0.293 \pm 0.011$. Replacing the information from the Union2.1 SN sample by the SNLS data leads to a change in the recovered values of about 1σ, with $w_{DE} = -1.071 \pm 0.055$ and $\Omega_m = 0.283 \pm 0.011$, showing a preference for values of $w_{DE} < -1$. As pointed out by Planck Collaboration XVI (2013), the difference between the results obtained using these samples might indicate that the treatment of the systematic errors affecting these SN data sets is incomplete.

Although exploring the constraints on a constant w_{DE} could indicate a deviation from the standard ΛCDM paradigm, more general dark energy models, such as those based on a scalar field, will be characterized by a time-dependent equation of state (e.g. Wetterich 1988). We explore the constraints on the time dependence of w_{DE}, parametrized as in equation (17). The blue dashed lines in Fig. 6 correspond to the two-dimensional marginalized constraints in the $w_0 - w_a$ plane obtained from the ePlanck CMB, covering a large region of the parameter space. The red solid lines in Fig. 6 correspond to the results obtained by combining the ePlanck CMB measurements with our BOSS $\xi_{\Delta\mu}(s)$ data set, showing a significant reduction of the allowed region for these parameters. In this case, we find $w_0 = -0.83^{+0.38}_{-0.34}$ and $w_a = -0.61^{+0.89}_{-0.96}$. As shown by the green dot–dashed lines in the same figure, the information from our Full data set combination tightens the constraints, leading to $w_0 = -0.95 \pm 0.14$ and $w_a = -0.29 \pm 0.47$, in agreement with the standard ΛCDM model values indicated by the dotted lines.

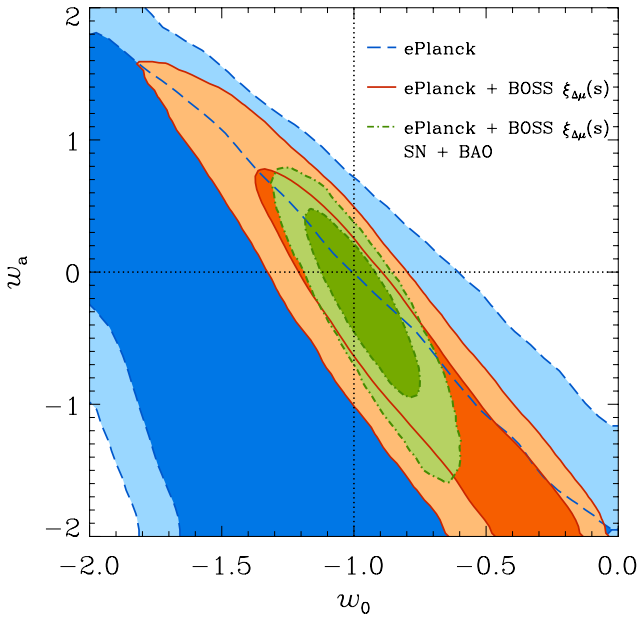

Figure 6. Marginalized 68 and 95 per cent CL in the $w_0 - w_a$ plane when we explore the redshift dependence of the dark energy equation of state, parametrized as in equation (17). The contours show the results obtained using the ePlanck CMB data alone (blue dashed lines), the ePlanck+BOSS $\xi_{\Delta\mu}(s)$ combination (red solid lines), and when this information is combined with our BAO and SN data sets (green dot–dashed lines). The dotted lines correspond to the fiducial values of these parameters in the ΛCDM model, $w_0 = -1$ and $w_a = 0$.

4.3 Non-flat universes

The standard ΛCDM model assumes a flat universe. Here we test this assumption by adding Ω_k to the list of free parameters of our base model. The blue dashed contours in Fig. 7 show the 68 and 95 per cent marginalized constraints in the $\Omega_m - \Omega_k$ plane derived by means of the ePlanck CMB data combination, which exhibit the so-called geometrical degeneracy (Efstathiou & Bond 1999) relating models with the same angular scale of the acoustic peaks in the CMB. This degeneracy extends over a wide range of values of Ω_k, leading to weak constraints on this parameter. In this case, we find

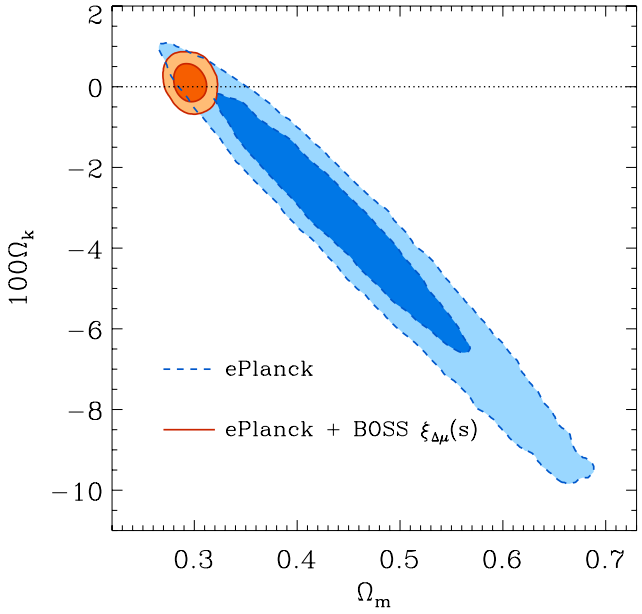

Figure 7. Marginalized constraints in the $\Omega_m - \Omega_k$ plane when the ΛCDM model is extended to allow for non-flat models. The contours show the 68 and 95 per cent CL obtained using the ePlanck CMB data alone (blue dashed lines) and the ePlanck+BOSS $\xi_{\Delta\mu}(s)$ combination (red solid lines). The dotted line corresponds to flat universes, with $\Omega_k = 0$.

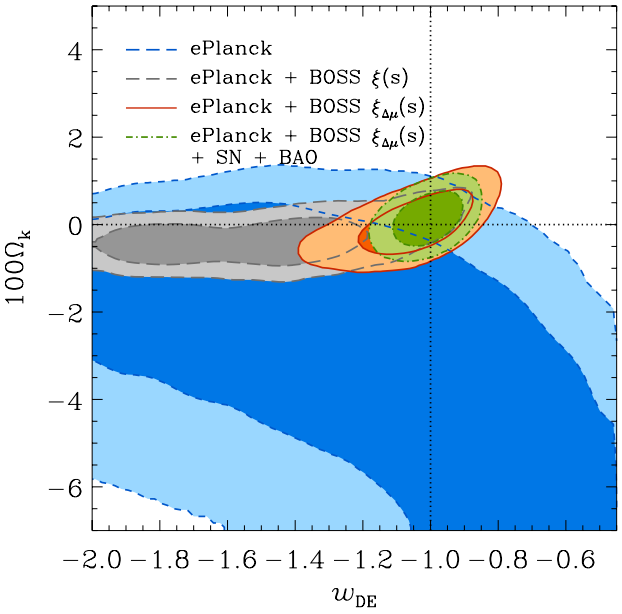

Figure 8. Marginalized constraints in the $w_{DE} - \Omega_k$ plane for the ΛCDM parameter set extended by allowing for simultaneous variations on both of these parameters. The contours correspond to the 68 and 95 per cent CL derived from the combination of ePlanck data alone (blue dashed lines), ePlanck plus the clustering wedges of the LOWZ and CMASS DR11 samples (red solid lines), and when the BAO and SN data sets are added to the latter combination (green dot–dashed lines). The dotted lines correspond to the values of these parameters in the ΛCDM model.

$100\Omega_k = -4.2^{+2.7}_{-1.7}$. As shown by Planck Collaboration XVI (2013), including information from the lensing signal inferred from the CMB partially reduces this degeneracy, but to obtain significantly tighter constraints it is necessary to combine these measurements with additional data sets.

When the ePlanck CMB data are combined with the monopole correlation functions of the DR11 LOWZ and CMASS samples, the constraints on D_V/r_d provided by these measurements are sufficient to break the geometrical degeneracy, leading to a constraint of $100\Omega_k = 0.07 \pm 0.31$, in excellent agreement with a flat Universe. The red solid lines in Fig. 7 show the constraints obtained when the ePlanck data are combined with the clustering wedges of these galaxy samples, leading to a similar result of $100\Omega_k = 0.10 \pm 0.29$. Including our SN and BAO data sets leads only to a small shift in the recovered mean value for this parameter, with $100\Omega_k = 0.15 \pm 0.29$, showing no evidence for a deviation from the flat Universe hypothesis, indicated by a dotted line in Fig. 7.

Both Ω_k and w_{DE} are involved in the geometrical degeneracy, as they change the distance to the last scattering surface. This means that when both of these parameters are varied simultaneously, the geometric degeneracy gains an extra degree of freedom, leading to a significant degradation of the obtained constraints. This effect is shown by the blue short-dashed contours in Fig. 8, which correspond to the constraints in the $w_{DE} - \Omega_k$ plane obtained from the ePlanck CMB data. In this case, the information from the LOWZ and CMASS angle-averaged correlation functions is not enough to break the geometric degeneracy completely (as shown by the grey long-dashed lines in Fig. 8). Although this information can constrain the curvature of the Universe to $100\Omega_k = -0.38^{+0.24}_{-0.28}$, it leaves a wide range of allowed values for the dark energy equation of state in the region where $w_{DE} < -1$.

The red solid contours in Fig. 8 correspond to constraints obtained after combining the ePlanck CMB data with the full shape of the clustering wedges of the DR11 LOWZ and CMASS samples. The additional information in the clustering wedges reduces the allowed region of this parameter space significantly, leading to the constraints $100\Omega_k = 0.02 \pm 0.43$ and $w_{DE} = -1.05 \pm 0.11$. As shown by the green dot–dashed lines in Fig. 8, including the information from the SN and additional BAO measurements can improve the constraints even further, leading to $100\Omega_k = -0.14 \pm 0.33$ and $w_{DE} = -1.009^{+0.062}_{-0.060}$, in excellent agreement with the ΛCDM model. In particular, the constraints on the dark energy equation of state obtained in this case have a similar accuracy as those presented in Section 4.2 under the assumption of a flat universe.

4.4 Massive neutrinos and relativistic species

In recent years, neutrino oscillation experiments have measured non-zero mass-squared differences between neutrino flavours, implying that they are massive and contribute to the total energy budget of the Universe. However, absolute neutrino mass measurements are more difficult to perform in the laboratory (Lobashev 2003; Eitel 2005; Otten & Weinheimer 2008) and current constraints are weaker than those imposed by cosmological observations such as CMB and LSS measurements (Lesgourgues & Pastor 2012).

Following the analysis of Planck Collaboration XVI (2013), our base ΛCDM model includes a non-zero contribution from massive neutrinos with $\sum m_\nu = 0.06\,\mathrm{eV}$ to the total energy budget of the Universe. In this section, we allow this parameter to vary freely assuming three neutrino species of equal mass and explore the constraints that can be imposed on this quantity by means of our DR11 clustering measurements.

The CMB power spectrum is sensitive to neutrino masses through two main effects, the change in the signal of the integrated Sachs–Wolfe effect at low multipoles and the lensing contribution at high ℓ

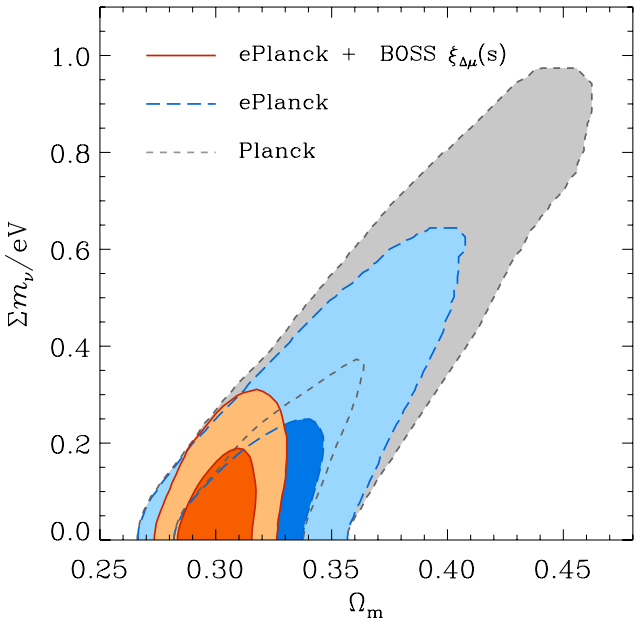

Figure 9. Marginalized constraints in the $\Omega_m - \Sigma m_\nu$ plane obtained when the ΛCDM parameter set is extended by treating the neutrino mass as a free parameter. The short- and long-dashed lines correspond to the 68 and 95 per cent CL derived by the *Planck* and ePlanck CMB data, respectively. The solid lines show the results obtained from the combination of the ePlanck CMB measurements with the full shape of the LOWZ and CMASS clustering wedges (red solid lines).

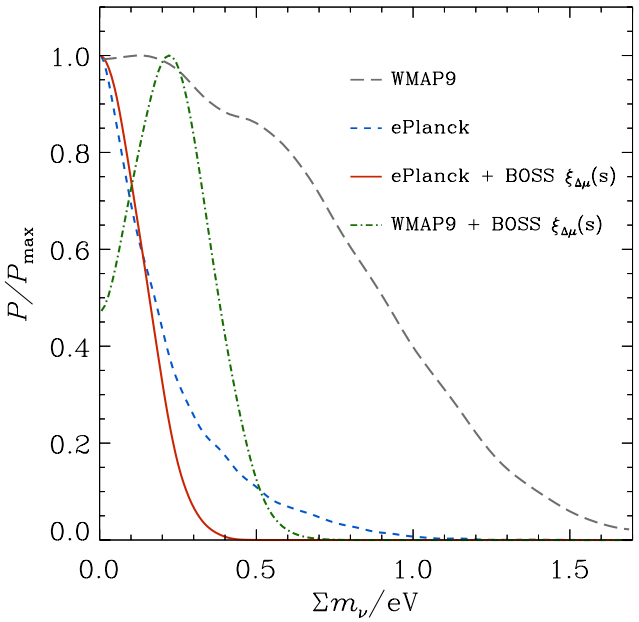

Figure 10. One-dimensional marginalized constraints on $\sum m_\nu$ obtained by means of the ePlanck CMB measurements (blue short-dashed line) and the combination of these data with the BOSS $\xi_{\Delta\mu}(s)$ (red solid line). The grey long-dashed and green dot–dashed lines correspond to the results obtained when the ePlanck CMB measurements are replaced by *WMAP*9.

(for a detailed description of these effects, see e.g. Lesgourgues & Pastor 2012; Lesgourgues et al. 2013; Hou et al. 2014). The grey short-dashed lines in Fig. 9 correspond to the 68 and 95 per cent CL in the $\Omega_m - \sum m_\nu$ plane derived from the *Planck* CMB data. These constraints are elongated along a line that corresponds to models with a constant redshift of matter-radiation equality, z_{eq}, which is accurately measured from CMB observations (Komatsu et al. 2009). As indicated by the blue long-dashed lines in the same figure, extending these data with the high-ℓ CMB measurements from ACT and SPT improves the results significantly, but leaves a residual degeneracy that limits the constraints on $\sum m_\nu$. This is shown by the blue short-dashed line in Fig. 10, which corresponds to the one-dimensional marginalized constraints on $\sum m_\nu$ obtained from the ePlanck CMB data, corresponding to $\sum m_\nu < 0.66$ eV (95 per cent CL).

The constraints on the total neutrino mass can be improved by combining the CMB information with our isotropic and anisotropic galaxy clustering measurements. As this information improves the constraints on Ω_m, it can break the degeneracy present in the CMB-only constraints. This effect is illustrated by the red solid lines in Fig. 9, which correspond to the results derived from our ePlanck + BOSS $\xi_{\Delta\mu}(s)$ combination. The effect of the extra information from BOSS on the constraints on the neutrino mass is shown by the red solid line in Fig. 10. In this case, we obtain the limit $\sum m_\nu < 0.24$ eV (95 per cent CL). As shown in Table 5, combining the CMB information with the LOWZ and CMASS angle-averaged correlation functions leads to a similar constraint. This limit is not improved by including the additional BAO and Union2.1 SN information in the analysis, in which case we obtain $\sum m_\nu < 0.23$ eV (95 per cent CL). When the SNLS SN compilation is used instead of the Union2.1 sample, we find a slightly tighter constraint, with $\sum m_\nu < 0.21$ eV (95 per cent CL).

The grey long-dashed lines in Fig. 10 correspond to the marginalized constraints on Σm_ν obtained using *WMAP*9 data alone, which extend over a wide range of allowed values. The green dot–dashed line shows the result obtained when the *WMAP*9 data are combined with the LOWZ and CMASS DR11 clustering wedges. Interestingly, in this case the constraints show a preference for a non-zero value of $\Sigma m_\nu \simeq 0.2$ eV. This is due to a slight difference in the values of z_{eq} preferred by the *Planck* and *WMAP*9 data. When using *WMAP*9 data, the degeneracy seen in Fig. 9 is shifted towards lower values of Ω_m. Adding the information from the clustering wedges measured from BOSS helps to tighten the constraints on the matter density, breaking the degeneracy obtained from the CMB at a region that shows a slight preference for non-zero values of Σm_ν.

The constraints on the total neutrino mass derived from cosmological observations are model dependent, as they vary depending on the parameter space being studied (Zhao et al. 2013). For example, if the dark energy equation of state is allowed to vary, the degeneracy in the CMB constraints gains an extra degree of freedom. This behaviour can be seen in the blue dashed contours of Fig. 11, which correspond to the two-dimensional marginalized constraints in the $w_{DE} - \sum m_\nu$ plane derived from the ePlanck data set. As shown by the grey long-dashed lines, in this parameter space the information provided by our BOSS $\xi(s)$ measurements cannot break the CMB degeneracy efficiently, leading to poor marginalized constraints. The additional information in the full shape of the clustering wedges reduces the allowed region for these parameters significantly, leading to the limit $\sum m_\nu < 0.47$ eV (95 per cent CL) and $w_{DE} = -1.13 \pm 0.12$. After also including the BAO and SN information, the constraints on the neutrino mass are improved to $\sum m_\nu < 0.33$ eV (95 per cent CL). This demonstrates that, when the uncertainties in the exact value of w_{DE} are taken into account, the upper bound on $\sum m_\nu$ is increased by 50 per cent with respect to the one obtained under the assumption of a ΛCDM model.

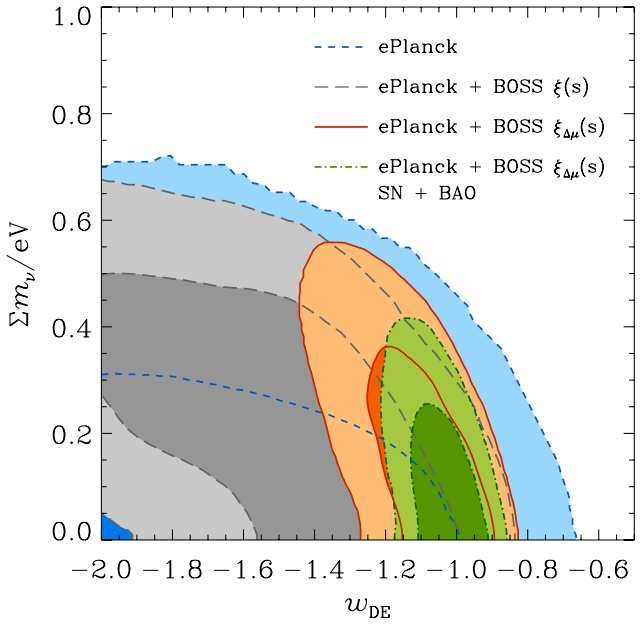

Figure 11. Marginalized constraints in the $w_{\rm DE}-\Sigma m_\nu$ plane obtained when the ΛCDM parameter set is extended by treating these quantities as free parameters. The contours correspond to the 68 and 95 per cent CL derived by the ePlanck CMB data alone (blue short-dashed lines) and the ePlanck+BOSS $\xi(s)$ (grey long-dashed lines), ePlanck+BOSS $\xi_{\Delta\mu}(s)$ (red solid lines) and Full data combinations (green dot–dashed lines).

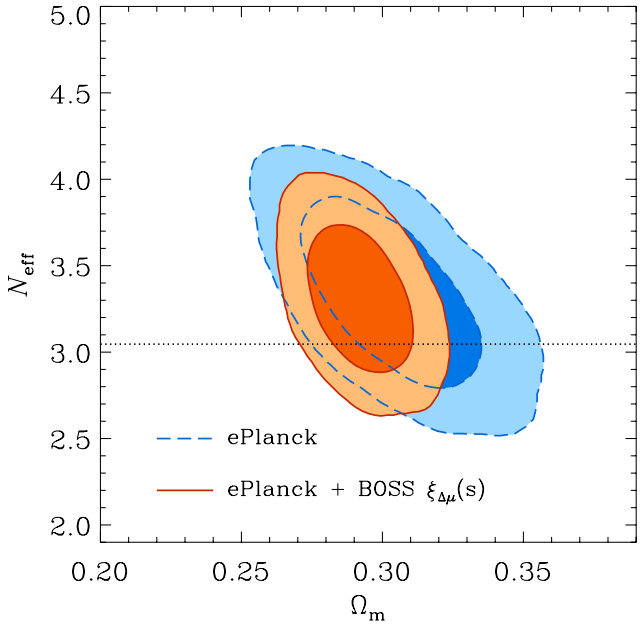

Figure 12. Marginalized constraints in the $\Omega_{\rm m}-N_{\rm eff}$ plane obtained when the ΛCDM parameter set is extended by treating the effective number of relativistic species as a free parameter. The dashed and solid lines correspond to the 68 and 95 per cent CL derived by the ePlanck CMB data and its combination with the full shape of the DR11 LOWZ and CMASS clustering wedges. The dotted line indicates the standard value of $N_{\rm eff}=3.046$.

It is also interesting to explore for potential deviations on the effective number of relativistic species from its standard value $N_{\rm eff}=3.046$. For this analysis, we extend the ΛCDM parameter space including $N_{\rm eff}$ as a free parameter, while assuming that the additional relativistic species are massless. As discussed in Planck Collaboration XVI (2013), the ePlanck CMB combination can place tight constraints on this parameter. These constraints are shown by the blue dashed lines in Fig. 12 which correspond to our ePlanck constraints in the $\Omega_{\rm m}-N_{\rm eff}$ plane, leading to $N_{\rm eff}=3.35\pm0.33$. Adding the information from the LOWZ and CMASS angle-averaged correlation functions leads to an improvement of this limit, with $N_{\rm eff}=3.31\pm0.27$. Using the information from our BOSS $\xi_{\Delta\mu}(s)$ or adding the information from the BAO and SN data leaves this result essentially unchanged.

4.5 Constraining deviations from GR

In Sections 4.1–4.4, we computed the logarithmic growth $f(z)$ required for our model of the full shape of the clustering wedges in the context of GR. Here we relax this assumption and parametrize its redshift evolution as $f(z)=\Omega_{\rm m}(z)^\gamma$, with the exponent γ treated as a free parameter. As described in Linder & Cahn (2007), GR predicts a value of $\gamma\simeq0.55$, with small corrections depending on the value of $w_{\rm DE}$. Then, the constraints on this parameter from the full shape of the LOWZ and CMASS clustering wedges can be used to set limits on potential deviations from the predictions of GR (Guzzo et al. 2008). This analysis is only possible using anisotropic clustering measurements such as the clustering wedges, as the effect of $f(z)$ and the bias parameter is degenerate in angle-averaged quantities.

The blue short-dashed line in Fig. 13 corresponds to the one-dimensional marginalized constraints on γ obtained from the combination of the *Planck* CMB measurements with the DR11 CMASS $\xi_\Delta(s)$. In this case, we obtain $\gamma=0.77\pm0.20$. Although a wide

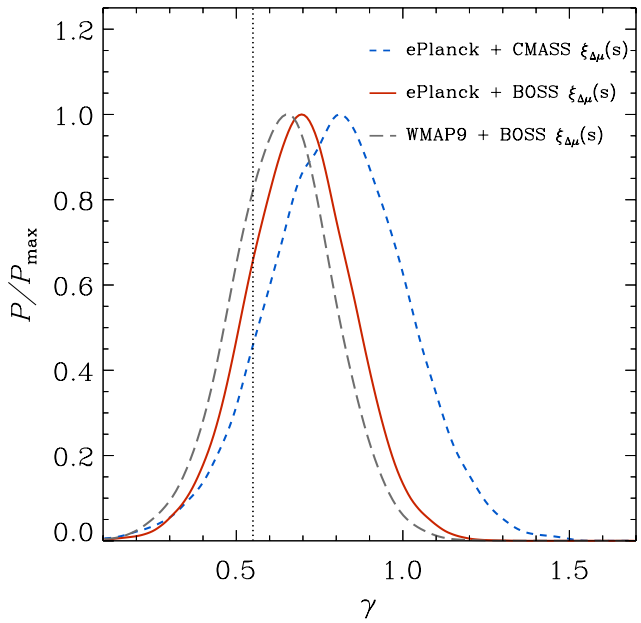

Figure 13. One-dimensional marginalized constraints on the power-law index of the structure growth-rate parameter, assuming $f(z)=\Omega_{\rm m}^\gamma$. The blue dashed lines correspond to the results obtained by combining the ePlanck CMB data with the DR11 CMASS clustering wedges. The red solid line shows the improvement obtained by including the information of the clustering wedges of the LOWZ sample in the analysis. Replacing the ePlanck CMB measurements by the *WMAP*9 data leads to similar constraints (grey dashed lines).

range of values of this parameter are allowed by the data, these results are consistent within 1σ with the predictions from GR, indicated by the dotted line. As shown by the red solid line, adding the information from the clustering wedges of the LOWZ sample improves the constraints to $\gamma = 0.69 \pm 0.15$, which illustrates the importance of including the low-redshift measurements. As shown in Table 5, these constraints are not modified when the *Planck* data are extended with the high-ℓ CMB measurements, or when the BAO and SN data sets are included in the analysis. The grey long-dashed line in Fig. 13 shows the constraints obtained by means of the *WMAP*9+BOSS $\xi_{\Delta}(s)$ combination, which leads to a constraint of $\gamma = 0.64 \pm 0.15$, in good agreement with the result obtained using the data from the *Planck* satellite.

Our constraints are in good agreement with those inferred in our companion papers. Samushia et al. (2014) use the full shape of the CMASS monopole–quadrupole pair in combination with recent CMB measurements to find $\gamma = 0.69 \pm 0.11$, while Beutler et al. (2013) derive a constraint of $\gamma = 0.772^{+0.124}_{-0.097}$ from the combination of *Planck* data with the multipoles of the CMASS power spectrum.

We also tested the effect of allowing for simultaneous variations of $w_{\rm DE}$ (assumed to be time independent) and γ. Fig. 14 presents the two-dimensional marginalized constraints in the $w_{\rm DE}-\gamma$ plane obtained in this case by means of the ePlanck + BOSS $\xi_{\Delta\mu}(s)$ combination (solid lines), and when these data are combined with the BAO and SN data sets (dot–dashed lines). Including γ as a free parameter leads to a degeneracy between this quantity and the dark energy equation of state, degrading the constraints on these parameters. In this case, we find $w_{\rm DE} = -1.15 \pm 0.11$ and $\gamma = 0.88 \pm 0.22$. As discussed in Sánchez et al. (2013), assuming that $f(z_{\rm m})$ follows the predictions of GR implies that the relative amplitude of $\xi_{\perp}(s)$ and $\xi_{\parallel}(s)$ provides information on $\Omega_{\rm m}$ that improves the obtained constraints. However, when this assumption is relaxed including γ as a free parameter, this extra constraining power is lost, leading to weaker limits. Including the SN and additional BAO measurements reduces the degeneracy present in the CMB + BOSS $\xi_{\Delta\mu}(s)$ constraints, leading to $w_{\rm DE} = -1.055 \pm 0.057$ and $\gamma = 0.75 \pm 0.17$, in agreement with the results obtained when these parameters are varied separately.

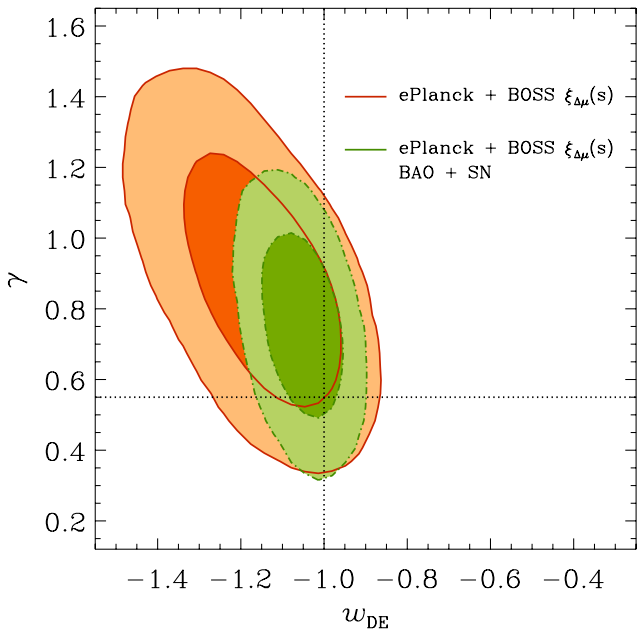

Figure 14. Marginalized constraints in the $w_{\rm DE}-\gamma$ plane obtained when the ΛCDM parameter set is extended by treating these quantities as free parameters. The red solid lines correspond to the 68 and 95 per cent CL obtained by combining the ePlanck CMB data with the DR11 LOWZ and CMASS clustering wedges. The green dot–dashed lines show the result of including the additional BAO and SN data sets in the analysis.

5 CONCLUSIONS

We have analysed the cosmological implications of the angle-averaged correlation functions, $\xi(s)$, and the clustering wedges, $\xi_{\perp}(s)$ and $\xi_{\parallel}(s)$, of the LOWZ and CMASS samples corresponding to SDSS-DR10 and DR11. We use a simple parametrization, based on RPT, as a tool to extract cosmological information from the full shape of these measurements for $s \gtrsim 40\ h^{-1}$ Mpc. We combine this information with CMB, SN and additional BAO measurements to derive constraints on the parameters of the standard ΛCDM model and a number of potential extensions, including curvature, alternative dark energy models, massive neutrinos, additional relativistic species and deviations from the predictions of GR. As shown by Sánchez et al. (2013), we find that the extra information provided by the clustering wedges is most useful when the dark energy equation of state is treated as a free parameter.

The constraints on $H(z)$ and $D_{\rm A}(z)$ from the clustering wedges are consistent with the predictions of the best-fitting ΛCDM model to the *Planck* CMB measurements. Assuming that the growth of structures follows the predictions of GR, the full shape of the LOWZ clustering wedges implies $D_{\rm A}(z_{\rm m}) = (965 \pm 37)(r_{\rm d}/r_{\rm d}^{\rm fid})$ Mpc and $H(z_{\rm m}) = (82.5 \pm 3.5)(r_{\rm d}^{\rm fid}/r_{\rm d})\,{\rm km\,s^{-1}\,Mpc^{-1}}$ at the mean redshift $z_{\rm m} = 0.32$, while the CMASS results give $D_{\rm A}(z_{\rm m}) = (1387 \pm 22)(r_{\rm d}/r_{\rm d}^{\rm fid})$ Mpc and $H(z_{\rm m}) = (94.3 \pm 2.4)(r_{\rm d}^{\rm fid}/r_{\rm d})\,{\rm km\,s^{-1}\,Mpc^{-1}}$ at $z_{\rm m} = 0.57$. Relaxing the assumption of GR, we find the marginalized constraints of $f\sigma_8(z = 0.32) = 0.48 \pm 0.10$ and $f\sigma_8(z = 0.57) = 0.417 \pm 0.045$. These values are in good agreement with those reported in our companion papers (Beutler et al. 2013; Chuang et al. 2013b; Samushia et al. 2014; Anderson et al. 2013), indicating the robustness of our results with respect to details in the methodology implemented in the analysis.

As can be seen in Table 5, our results show no significant evidence for a deviation from the standard ΛCDM model, which provides a good description of the full shape of all our clustering measurements. In particular, the ePlanck+BOSS $\xi_{\Delta\mu}(s)$ combination alone is sufficient to constrain the curvature of the Universe to $\Omega_k = 0.0010 \pm 0.0029$, the total neutrino mass to $\sum m_\nu < 0.24$ eV (95 per cent CL), the effective number of relativistic species to $N_{\rm eff} = 3.31 \pm 0.27$ and the dark energy equation of state to $w_{\rm DE} = -1.051 \pm 0.076$. Adding the information from our BAO and SN data sets further improves these constraints.

The assumption that the dark energy component can be characterized by a constant equation of state specified by $w_{\rm DE}(z) = -1$ has strong implications on the constraints obtained in several parameter spaces. Allowing this parameter to vary weakens the constraints obtained from the combination of CMB information with our BOSS $\xi(s)$ measurements. These cases illustrate the extra constraining power of the clustering wedges, which lead in general to similar constraints to the ones derived under the assumption that dark energy behaves as a cosmological constant.

The information from the full shape of the clustering wedges can be used to constrain potential deviations from the predictions of GR. Assuming that $f(z) = \Omega_{\rm m}(z)^{\gamma}$, the combination of the ePlanck CMB measurements with the DR11 LOWZ and CMASS clustering wedges gives a constraint of $\gamma = 0.69 \pm 0.15$, consistent with no deviation from the GR prediction of $\gamma = 0.55$ within 1σ. The

assumption that $f(z)$ follows the predictions of GR implies that the relative amplitude of the clustering wedges contains information on $\Omega_{\rm m}$. When this assumption is relaxed, this additional constraining power is lost, affecting the constraints on other parameters. For example, if γ and $w_{\rm DE}$ are varied simultaneously, the ePlanck+BOSS $\xi_{\Delta\mu}(s)$ combination implies that $\gamma = 0.88 \pm 0.22$ and $w_{\rm DE} = -1.15 \pm 0.11$. When the additional BAO and Union2.1 SN measurements are included in the analysis, we find $w_{\rm DE} = -1.055 \pm 0.057$ and $\gamma = 0.75 \pm 0.17$, in agreement with the results obtained when these parameters are varied separately.

Combining our clustering measurements with the *WMAP*9 or *Planck* CMB measurements leads to results that, although consistent, differ at the 1σ level. This highlights the importance of a detailed analysis of the origin of the differences between *WMAP*9 and *Planck* as these could indicate the presence of systematic errors. Similar differences are observed when the Union2.1 SN compilation is replaced by the SNLS sample, which leads to changes in the obtained constraints of the same order or larger than the associated statistical errors. This situation might change in the near future, as results based on new calibrations of these SN samples (Betoule et al. 2013) become available.

As SDSS-III approaches the end of observations in 2014 June, the galaxy and quasar samples from BOSS are close to being completed. Besides the improvement in the statistical power of the final data sets, these samples will allow us to perform an improved analysis of the potential systematic errors affecting our measurements. The final galaxy samples from BOSS will deliver the most accurate views of the LSS of the Universe at $z < 0.7$, thus providing invaluable cosmological information.

ACKNOWLEDGEMENTS

We would like to thank the referee, Will Sutherland, for his careful reading of our manuscript and his suggestions to improve the quality of the publication. AGS would like to thank Ximena Mazzalay for useful discussions. AGS and FM acknowledge support from the Trans-regional Collaborative Research Centre TR33 'The Dark Universe' of the German Research Foundation (DFG). EK is supported by the Australian Research Council Centre of Excellence for All-sky Astrophysics (CAASTRO), through project number CE110001020.

Numerical computations for the PTHALOS mocks were done on the Sciama High Performance Compute (HPC) cluster which is supported by the ICG, SEPNet and the University of Portsmouth.

Funding for SDSS-III has been provided by the Alfred P. Sloan Foundation, the Participating Institutions, the National Science Foundation and the US Department of Energy.

SDSS-III is managed by the Astrophysical Research Consortium for the Participating Institutions of the SDSS-III Collaboration including the University of Arizona, the Brazilian Participation Group, Brookhaven National Laboratory, University of Cambridge, Carnegie Mellon University, University of Florida, the French Participation Group, the German Participation Group, Harvard University, the Instituto de Astrofisica de Canarias, the Michigan State/Notre Dame/JINA Participation Group, Johns Hopkins University, Lawrence Berkeley National Laboratory, Max Planck Institute for Astrophysics, Max Planck Institute for Extraterrestrial Physics, New Mexico State University, New York University, Ohio State University, Pennsylvania State University, University of Portsmouth, Princeton University, the Spanish Participation Group, University of Tokyo, University of Utah, Vanderbilt University, University of Virginia, University of Washington and Yale University.

This work is based on observations obtained with *Planck* (http://www.esa.int/Planck), an ESA science mission with instruments and contributions directly funded by ESA Member States, NASA and Canada. We acknowledge the use of the Legacy Archive for Microwave Background Data Analysis (LAMBDA). Support for LAMBDA is provided by the NASA Office of Space Science.

REFERENCES

Ahn C. P. et al., 2012, ApJS, 203, 21
Ahn C. P. et al., 2013, preprint (arXiv:1307.7735)
Aihara H. et al., 2011, ApJS, 193, 29
Alcock C., Paczynski B., 1979, Nature, 281, 358
Anderson L. et al., 2012, MNRAS, 427, 3435
Anderson L. et al., 2013, MNRAS, preprint (arXiv:1312.4877)
Anderson L. et al., 2014, MNRAS, 439, 83
Angulo R. E., Baugh C. M., Frenk C. S., Lacey C. G., 2008, MNRAS, 383, 755
Ballinger W. E., Peacock J. A., Heavens A. F., 1996, MNRAS, 282, 877
Bennett C. L. et al., 2013, ApJS, 208, 20
Betoule M. et al., 2013, A&A, 552, A124
Beutler F. et al., 2011, MNRAS, 416, 3017
Beutler F. et al., 2013, MNRAS, preprint (arXiv:1312.4611)
Blake C., Glazebrook K., 2003, ApJ, 594, 665
Blake C. et al., 2011, MNRAS, 418, 1707
Blake C. et al., 2012, MNRAS, 425, 405
Bolton A. S. et al., 2012, AJ, 144, 144
Busca N. G. et al., 2013, A&A, 552, A96
Cabré A., Gaztañaga E., 2009, MNRAS, 393, 1183
Chevallier M., Polarski D., 2001, Int. J. Mod. Phys. D, 10, 213
Chuang C.-H. et al., 2013a, MNRAS, 433, 3559
Chuang C.-H. et al., 2013b, MNRAS, preprint (arXiv:1312.4889)
Cole S., Fisher K. B., Weinberg D. H., 1995, MNRAS, 275, 515
Cole S. et al., 2005, MNRAS, 362, 505
Colless M. et al., 2001, MNRAS, 328, 1039
Colless M. et al., 2003, preprint (astro-ph/0306581)
Conley A. et al., 2011, ApJS, 192, 1
Crocce M., Scoccimarro R., 2006, Phys. Rev. D, 73, 063519
Crocce M., Scoccimarro R., 2008, Phys. Rev. D, 77, 023533
Das S. et al., 2013, preprint (arXiv:1301.1037)
Dawson K. S. et al., 2013, AJ, 145, 10
Drinkwater M. J. et al., 2010, MNRAS, 401, 1429
Efstathiou G., Bond J. R., 1999, MNRAS, 304, 75
Eisenstein D. J., Hu W., 1998, ApJ, 496, 605
Eisenstein D. J. et al., 2001, AJ, 122, 2267
Eisenstein D. J. et al., 2005, ApJ, 633, 560
Eisenstein D. J., Seo H.-J., Sirko E., Spergel D. N., 2007, ApJ, 664, 675
Eisenstein D. J. et al., 2011, AJ, 142, 72
Eitel K., 2005, Nucl. Phys. B: Proc. Suppl., 143, 197
Fang W., Hu W., Lewis A., 2008, Phys. Rev. D, 78, 087303
Feldman H. A., Kaiser N., Peacock J. A., 1994, ApJ, 426, 23
Frieman J. A., Turner M. S., Huterer D., 2008, ARA&A, 46, 385
Gunn J. E. et al., 1998, AJ, 116, 3040
Gunn J. E. et al., 2006, AJ, 131, 2332
Guzzo L. et al., 2008, Nature, 451, 541
Hamilton A. J. S., 1997, MNRAS, 289, 295
Hartlap J., Simon P., Schneider P., 2007, A&A, 464, 399
Hinshaw G. et al., 2013, ApJS, 208, 19
Hou Z. et al., 2014, ApJ, 782, 74
Hu W., Haiman Z., 2003, Phys. Rev. D, 68, 063004
Hu W., Sawicki I., 2007, Phys. Rev. D, 76, 104043
Jackson J. C., 1972, MNRAS, 156, 1p
Jones D. H. et al., 2009, MNRAS, 399, 683
Kazin E. A., Sánchez A. G., Blanton M. R., 2012, MNRAS, 419, 3223
Kazin E. A. et al., 2013, MNRAS, 435, 64
Keisler R. et al., 2011, ApJ, 743, 28
Kirkby D. et al., 2013, J. Cosmol. Astropart. Phys., 3, 24

Komatsu E. et al., 2009, ApJS, 180, 330
Kowalski M. et al., 2008, ApJ, 686, 749
Landy S. D., Szalay A. S., 1993, ApJ, 412, 64
Lesgourgues J., Pastor S., 2012, Phys. Rep., 429, 307
Lesgourgues J., Mangano G., Miele G., Pastor S., 2013, Neutrino Cosmology. Cambridge Univ. Press, Cambridge
Lewis A., Bridle S., 2002, Phys. Rev. D, 66, 103511
Lewis A., Challinor A., Lasenby A., 2000, ApJ, 538, 473
Linder E. V., 2003, Phys. Rev. D, 68, 083504
Linder E. V., Cahn R. N., 2007, Astropart. Phys., 28, 481
Lobashev V. M., 2003, Nucl. Phys. A, 719, 153
Manera M. et al., 2013, MNRAS, 428, 1036
Manera M. et al., 2014, MNRAS, preprint (arXiv:1401.4171)
Maraston C. et al., 2013, MNRAS, 435, 2764
Masters K. L. et al., 2011, MNRAS, 418, 1055
Matsubara T., 2004, ApJ, 615, 573
Meiksin A., White M., Peacock J. A., 1999, MNRAS, 304, 851
Montesano F., Sánchez A. G., Phleps S., 2010, MNRAS, 408, 2397
Montesano F., Sánchez A. G., Phleps S., 2012, MNRAS, 421, 2656
Nuza S. E. et al., 2013, MNRAS, 432, 743
Otten E. W., Weinheimer C., 2008, Rep. Prog. Phys., 71, 086201
Padmanabhan N. et al., 2007, MNRAS, 378, 852
Parejko J. K. et al., 2013, MNRAS, 429, 98
Park C., Vogeley M. S., Geller M. J., Huchra J. P., 1994, ApJ, 431, 569
Peebles P. J., Ratra B., 2003, Rev. Mod. Phys., 75, 559
Percival W. J. et al., 2002, MNRAS, 337, 1068
Percival W. J. et al., 2014, MNRAS, preprint (arXiv:1312.4841)
Planck Collaboration I, 2013, preprint (arXiv:1303.5062)
Planck Collaboration XVI, 2013, preprint (arXiv:1303.5076)
Reichardt C. L. et al., 2012, ApJ, 755, 70
Reid B. A. et al., 2012, MNRAS, 426, 2719
Ross A. J. et al., 2014, MNRAS, 437, 1109
Samushia L. et al., 2013, MNRAS, 429, 1514
Samushia L. et al., 2014, MNRAS, preprint (arXiv:1312.4899)
Sánchez A. G., Baugh C. M., Angulo R. E., 2008, MNRAS, 390, 1470
Sánchez A. G., Crocce M., Cabré A., Baugh C. M., Gaztañaga E., 2009, MNRAS, 400, 1643
Sánchez A. G. et al., 2012, MNRAS, 425, 415
Sánchez A. G. et al., 2013, MNRAS, 433, 1202
Scoccimarro R., Sheth R. K., 2002, MNRAS, 329, 629
Seo H.-J., Eisenstein D., 2003, ApJ, 598, 720
Seo H.-J. et al., 2012, ApJ, 761, 13
Slosar A. et al., 2013, J. Cosmol. Astropart. Phys., 4, 026
Smee S. A. et al., 2013, AJ, 146, 32
Smith R. E., Scoccimarro R., Sheth R. K., 2008, Phys. Rev. D, 77, 043525
Story K. T. et al., 2013, ApJ, 779, 86
Suzuki N. et al., 2012, ApJ, 746, 85
Taylor A., Joachimi B., Kitching T., 2013, MNRAS, 432, 1928
Thomas D. et al., 2013, MNRAS, 431, 1383
Tojeito R. et al., 2014, MNRAS, preprint (arXiv:1401.1768)
Vargas-Magaña M. et al., 2013, MNRAS, preprint (arXiv:1312.4996)
Wetterich C., 1988, Nucl. Phys. B, 302, 668
White M. et al., 2011, ApJ, 728, 126
Wishart J., 1928, Biometrika, 20A, 32
Xu X., Padmanabhan N., Eisenstein D. J., Mehta K. T., Cuesta A. J., 2012, MNRAS, 427, 2146
York D. G. et al., 2000, AJ, 120, 1579
Zhao G.-B. et al., 2013, MNRAS, 436, 2038

APPENDIX A: SUMMARY OF THE OBTAINED CONSTRAINTS

In this appendix, we summarize the constraints on cosmological parameters obtained using different combinations of the data sets described in Section 2. Tables A1–A9 list the 68 per cent confidence limits obtained in the parameter spaces analysed in Sections 4.1–4.5. The upper section of these tables lists the constraints on the main parameters included in the fits, while the lower section contains the results on the parameters derived from the first set.

Table A1. Marginalized 68 per cent constraints on the cosmological parameters of the standard ΛCDM model, obtained using different combinations of the data sets described in Section 2.

	ePlanck+BOSS $\xi(s)$	ePlanck+BOSS $\xi_{\Delta\mu}(s)$	ePlanck + BOSS $\xi_{\Delta\mu}(s)$ +BAO+SN
Main parameters			
$100\,\omega_{\rm b}$	2.2202 ± 0.024	2.226 ± 0.025	2.227 ± 0.024
$100\,\omega_{\rm c}$	11.78 ± 0.16	11.69 ± 0.17	11.66 ± 0.16
$10^4 \times \theta_{\rm MC}$	104.159 ± 0.056	104.169 ± 0.058	104.172 ± 0.056
$n_{\rm s}$	0.9628 ± 0.0052	0.9650 ± 0.0055	0.9651 ± 0.0052
$\ln(10^{10} A_{\rm s})$	3.089 ± 0.025	3.086 ± 0.027	3.087 ± 0.025
Derived parameters			
$100\Omega_{\rm DE}$	$69.78^{+0.96}_{-0.94}$	70.288 ± 0.99	70.47 ± 0.91
$100\Omega_{\rm m}$	$30.22^{+0.94}_{-0.96}$	29.712 ± 0.99	29.53 ± 0.91
σ_8	0.822 ± 0.011	0.818 ± 0.012	0.817 ± 0.011
h	$0.6823^{+0.0073}_{-0.0071}$	0.6862 ± 0.0077	0.6876 ± 0.0072
t_0/Gyr	13.784 ± 0.036	13.771 ± 0.037	13.768 ± 0.036

Table A2. Marginalized 68 per cent constraints on the cosmological parameters of the ΛCDM model extended by including $w_{\rm DE}$ (assumed constant) as a free parameter, obtained using different combinations of the data sets described in Section 2.

	ePlanck+BOSS $\xi(s)$	ePlanck+BOSS $\xi_{\Delta\mu}(s)$	ePlanck + BOSS $\xi_{\Delta\mu}(s)$ +BAO+SN
Main parameters			
$w_{\rm DE}$	$-1.31^{+0.21}_{-0.16}$	-1.051 ± 0.077	-1.024 ± 0.053
$100\,\omega_{\rm b}$	2.205 ± 0.025	2.2217 ± 0.025	2.224 ± 0.025
$100\,\omega_{\rm c}$	12.06 ± 0.23	11.76 ± 0.21	11.72 ± 0.20
$10^4 \times \theta_{\rm MC}$	104.121 ± 0.059	104.159 ± 0.060	104.166 ± 0.058
$n_{\rm s}$	0.9563 ± 0.0063	0.9630 ± 0.0062	0.9639 ± 0.0059
$\ln(10^{10}A_{\rm s})$	3.088 ± 0.024	3.085 ± 0.025	3.085 ± 0.024
Derived parameters			
$100\Omega_{\rm DE}$	$75.1^{+2.6}_{-3.4}$	71.2 ± 1.6	70.7 ± 1.2
$100\Omega_{\rm m}$	$24.9^{+3.4}_{-2.6}$	28.8 ± 1.6	29.2 ± 1.2
σ_8	$0.915^{+0.052}_{-0.061}$	0.834 ± 0.027	0.825 ± 0.021
h	$0.763^{+0.041}_{-0.056}$	$0.699^{+0.020}_{-0.021}$	0.692 ± 0.014
t_0/Gyr	$13.678^{+0.068}_{-0.063}$	13.753 ± 0.049	13.762 ± 0.040

Table A3. The marginalized 68 per cent constraints on the cosmological parameters of the ΛCDM model extended by allowing for variations on $w_{\rm DE}(a)$ (parametrized according to equation 17), obtained using different combinations of the data sets described in Section 2.

	ePlanck+BOSS $\xi(s)$	ePlanck+BOSS $\xi_{\Delta\mu}(s)$	ePlanck + BOSS $\xi_{\Delta\mu}(s)$ +BAO+SN
Main parameters			
w_0	$-1.29^{+0.50}_{-0.46}$	$-0.83^{+0.39}_{-0.34}$	-0.95 ± 0.14
w_a	$-0.2^{+1.0}_{-1.1}$	$-0.61^{+0.90}_{-0.98}$	$-0.29^{+0.48}_{-0.49}$
$100\,\omega_{\rm b}$	2.206 ± 0.025	2.219 ± 0.025	2.221 ± 0.025
$100\,\omega_{\rm c}$	12.04 ± 0.23	11.80 ± 0.20	11.76 ± 0.20
$10^4 \times \theta_{\rm MC}$	$104.122^{+0.059}_{-0.057}$	104.151 ± 0.060	104.158 ± 0.060
$n_{\rm s}$	$0.9565^{+0.0063}_{-0.0064}$	0.9618 ± 0.0062	0.9628 ± 0.0062
$\ln(10^{10}A_{\rm s})$	3.087 ± 0.024	3.084 ± 0.025	3.083 ± 0.025
Derived parameters			
$100\Omega_{\rm DE}$	$74.8^{+4.9}_{-5.3}$	$69.1^{+3.6}_{-4.1}$	70.5 ± 1.3
$100\Omega_{\rm m}$	$25.2^{+5.3}_{-4.9}$	$30.9^{+4.1}_{-3.6}$	29.5 ± 1.3
σ_8	$0.912^{+0.068}_{-0.071}$	$0.821^{+0.38}_{-0.39}$	0.827 ± 0.022
h	0.763 ± 0.079	$0.679^{+0.039}_{-0.045}$	0.690 ± 0.014
t_0/Gyr	$13.683^{+0.069}_{-0.070}$	13.753 ± 0.054	13.748 ± 0.049

Table A4. Marginalized 68 per cent constraints on the cosmological parameters of the ΛCDM model extended by including non-flat models, obtained using different combinations of the data sets described in Section 2.

	ePlanck+BOSS $\xi(s)$	ePlanck+BOSS $\xi_{\Delta\mu}(s)$	ePlanck + BOSS $\xi_{\Delta\mu}(s)$ +BAO+SN
Main parameters			
$100\,\Omega_k$	0.07 ± 0.31	0.10 ± 0.29	0.15 ± 0.29
$100\,\omega_{\rm b}$	2.218 ± 0.027	2.223 ± 0.027	2.222 ± 0.028
$100\,\omega_{\rm c}$	11.83 ± 0.26	11.75 ± 0.25	11.77 ± 0.24
$10^4 \times \theta_{\rm MC}$	104.150 ± 0.060	104.160 ± 0.063	104.158 ± 0.063
$n_{\rm s}$	0.9618 ± 0.0070	0.9632 ± 0.0069	0.9630 ± 0.0068
$\ln(10^{10}A_{\rm s})$	3.089 ± 0.024	3.085 ± 0.025	3.086 ± 0.025
Derived parameters			
$100\Omega_{\rm DE}$	69.75 ± 0.97	$70.3^{+0.9}_{-1.0}$	$70.38^{+0.92}_{-0.93}$
$100\Omega_{\rm m}$	30.18 ± 0.96	29.6 ± 1.0	$29.47^{+0.94}_{-0.91}$
σ_8	0.824 ± 0.013	0.820 ± 0.013	0.821 ± 0.013
h	$0.6839^{+0.0096}_{-0.0094}$	0.6890 ± 0.010	0.6908 ± 0.0096
t_0/Gyr	13.75 ± 0.12	13.73 ± 0.12	13.71 ± 0.12

Table A5. The marginalized 68 per cent constraints on the cosmological parameters of the ΛCDM model extended by allowing for simultaneous variations on $w_{\rm DE}$ and Ω_k, obtained using different combinations of the data sets described in Section 2.

	ePlanck+BOSS $\xi(s)$	ePlanck+BOSS $\xi_{\Delta\mu}(s)$	ePlanck + BOSS $\xi_{\Delta\mu}(s)$ +BAO+SN
Main parameters			
$100\Omega_k$	$-0.38^{+0.22}_{-0.24}$	0.02 ± 0.43	0.14 ± 0.34
$w_{\rm DE}$	$-1.53^{+0.24}_{-0.28}$	-1.05 ± 0.11	-1.009 ± 0.063
$100\,\omega_{\rm b}$	2.222 ± 0.028	2.223 ± 0.028	2.221 ± 0.028
$100\,\omega_{\rm c}$	11.84 ± 0.25	11.76 ± 0.26	11.77 ± 0.25
$10^4 \times \theta_{\rm MC}$	104.153 ± 0.062	104.159 ± 0.063	104.156 ± 0.063
$n_{\rm s}$	$0.9610^{+0.0068}_{-0.0067}$	$0.9631^{+0.0070}_{-0.0069}$	0.9629 ± 0.0070
$\ln(10^{10}A_{\rm s})$	3.085 ± 0.024	3.084 ± 0.025	3.085 ± 0.024
Derived parameters			
$100\Omega_{\rm DE}$	$78.4^{+3.9}_{-3.4}$	71.1 ± 2.3	70.5 ± 1.3
$100\Omega_{\rm m}$	$21.9^{+3.3}_{-3.9}$	28.9 ± 2.0	29.4 ± 1.2
σ_8	$0.961^{+0.073}_{-0.064}$	0.833 ± 0.033	0.823 ± 0.022
h	$0.810^{+0.075}_{-0.062}$	0.699 ± 0.023	0.692 ± 0.013
t_0/Gyr	13.84 ± 0.13	13.76 ± 0.15	13.71 ± 0.13

Table A6. Marginalized 68 per cent constraints on the ΛCDM model extended by treating $\sum m_\nu$ as a free parameter, obtained using different combinations of the data sets described in Section 2.

	ePlanck+BOSS $\xi(s)$	ePlanck+BOSS $\xi_{\Delta\mu}(s)$	ePlanck + BOSS $\xi_{\Delta\mu}(s)$ +BAO+SN
Main parameters			
$\sum m_\nu$	<0.23 eV (95% CL)	<0.24 eV (95% CL)	<0.23 eV (95% CL)
$100\,\omega_{\rm b}$	2.221 ± 0.023	2.226 ± 0.024	2.228 ± 0.024
$100\,\omega_{\rm b}$	2.221 ± 0.023	2.226 ± 0.024	2.228 ± 0.024
$100\,\omega_{\rm c}$	11.76 ± 0.17	11.67 ± 0.18	11.64 ± 0.17
$10^4 \times \theta_{\rm MC}$	104.158 ± 0.056	104.170 ± 057	104.175 ± 0.056
$n_{\rm s}$	0.9631 ± 0.0054	0.9651 ± 0.0056	0.9656 ± 0.0054
$\ln(10^{10} A_{\rm s})$	3.089 ± 0.025	3.087 ± 0.026	3.088 ± 0.026
Derived parameters			
f_ν	<0.017 (95% CL)	<0.019 (95% CL)	<0.017 (95% CL)
$100\Omega_{\rm DE}$	69.6 ± 1.0	70.0 ± 1.0	70.3 ± 1.0
$100\Omega_{\rm m}$	30.4 ± 1.0	30.0 ± 1.0	29.7 ± 1.0
σ_8	0.816 ± 0.020	0.809 ± 0.021	0.811 ± 0.020
h	0.6808 ± 0.0082	$0.6840^{+0.0089}_{-0.0091}$	$0.6860^{+0.0085}_{-0.0086}$
t_0/Gyr	13.795 ± 0.046	13.79 ± 0.050	$13.78^{+0.0048}_{-0.0047}$

Table A7. The marginalized 68 per cent constraints on the cosmological parameters of the ΛCDM model extended by allowing for simultaneous variations on $\sum m_\nu$ and $w_{\rm DE}$, obtained using different combinations of the data sets described in Section 2.

	ePlanck+BOSS $\xi(s)$	ePlanck+BOSS $\xi_{\Delta\mu}(s)$	ePlanck + BOSS $\xi_{\Delta\mu}(s)$ +BAO+SN
Main parameters			
$\sum m_\nu$	<0.49 eV (95% CL)	<0.47 eV (95% CL)	<0.33 eV (95% CL)
$w_{\rm DE}$	$-1.49^{+0.24}_{-0.30}$	-1.13 ± 0.12	-1.046 ± 0.064
$100\,\omega_{\rm b}$	2.203 ± 0.024	2.219 ± 0.025	2.223 ± 0.025
$100\,\omega_{\rm c}$	12.03 ± 0.21	11.75 ± 0.20	11.70 ± 0.20
$10^4 \times \theta_{\rm MC}$	104.118 ± 0.058	104.150 ± 0.060	104.163 ± 0.059
$n_{\rm s}$	0.9565 ± 0.0060	0.9627 ± 0.0062	0.9642 ± 0.0059
$\ln(10^{10} A_{\rm s})$	3.090 ± 0.025	3.087 ± 0.026	3.087 ± 0.025
Derived parameters			
f_ν	<0.036 (95% CL)	<0.035 (95% CL)	<0.025 (95% CL)
$100\Omega_{\rm DE}$	$76.8^{+4.0}_{-3.1}$	71.6 ± 1.8	70.7 ± 1.2
$100\Omega_{\rm m}$	$23.2^{+3.1}_{-4.0}$	28.4 ± 1.8	29.3 ± 1.2
σ_8	0.910 ± 0.058	0.821 ± 0.031	0.815 ± 0.026
h	$0.796^{+0.076}_{-0.058}$	0.707 ± 0.025	0.693 ± 0.014
t_0/Gyr	$13.71^{+0.70}_{-0.69}$	13.79 ± 0.064	13.78 ± 0.054

Table A8. Marginalized 68 per cent constraints on the cosmological parameters of the ΛCDM model extended by including $N_{\rm eff}$ as a free parameter, obtained using different combinations of the data sets described in Section 2.

	ePlanck+BOSS $\xi(s)$	ePlanck+BOSS $\xi_{\Delta\mu}(s)$	ePlanck + BOSS $\xi_{\Delta\mu}(s)$ +BAO+SN
Main parameters			
$N_{\rm eff}$	3.35 ± 0.27	3.31 ± 0.27	3.30 ± 0.27
$100\,\omega_{\rm b}$	2.239 ± 0.030	2.243 ± 0.031	2.243 ± 0.029
$100\,\omega_{\rm c}$	12.25 ± 0.47	12.10 ± 0.46	12.07 ± 0.45
$10^4 \times \theta_{\rm MC}$	104.111 ± 0.072	104.126 ± 0.072	104.130 ± 0.072
$n_{\rm s}$	0.972 ± 0.010	0.973 ± 0.011	0.973 ± 0.010
$\ln(10^{10}A_{\rm s})$	3.108 ± 0.030	3.100 ± 0.029	3.101 ± 0.029
Derived parameters			
$100\Omega_{\rm DE}$	70.3 ± 1.0	70.8 ± 1.1	70.9 ± 1.0
$100\Omega_{\rm m}$	29.7 ± 1.0	29.2 ± 1.1	29.1 ± 1.0
σ_8	0.839 ± 0.019	0.831 ± 0.018	0.831 ± 0.018
h	0.701 ± 0.018	0.703 ± 0.019	0.703 ± 0.018
t_0/Gyr	13.50 ± 0.26	13.52 ± 0.26	13.53 ± 0.26

Table A9. The marginalized 68 per cent constraints on the parameters of the ΛCDM model extended by assuming $f(z_{\rm m}) = \Omega_{\rm m}(z)^{\gamma}$ and treating γ as a free parameter, and when γ and $w_{\rm DE}$ are varied simultaneously.

	ePlanck+BOSS $\xi_{\Delta\mu}(s)$	ePlanck + BOSS $\xi_{\Delta\mu}(s)$ +BAO+SN	ePlanck+BOSS $\xi_{\Delta\mu}(s)$	ePlanck + BOSS $\xi_{\Delta\mu}(s)$ +BAO+SN
Main parameters				
$w_{\rm DE}$	–	–	−1.16 ± 0.11	−1.055 ± 0.058
γ	0.69 ± 0.15	0.69 ± 0.15	0.89 ± 0.22	0.76 ± 0.17
$100\,\omega_{\rm b}$	2.225 ± 0.024	2.226 ± 0.024	2.213 ± 0.025	2.220 ± 0.025
$100\,\omega_{\rm c}$	11.70 ± 0.16	11.68 ± 0.016	11.91 ± 0.21	11.79 ± 0.20
$10^4 \times \theta_{\rm MC}$	104.169 ± 0.055	104.172 ± 0.055	104.141 ± 0.061	104.156 ± 0.057
$n_{\rm s}$	0.9644 ± 0.0055	0.9648 ± 0.0053	0.9594 ± 0.0062	0.9622 ± 0.0058
$\ln(10^{10}A_{\rm s})$	3.090 ± 0.025	3.091 ± 0.025	3.088 ± 0.025	3.088 ± 0.025
Derived parameters				
$100\Omega_{\rm DE}$	$0.7024^{+0.0092}_{-0.0095}$	0.7038 ± 0.0090	0.728 ± 0.021	0.711 ± 0.012
$100\Omega_{\rm m}$	$0.2976^{+0.0095}_{-0.0092}$	0.2962 ± 0.0090	0.272 ± 0.021	0.289 ± 0.012
σ_8	0.820 ± 0.011	0.820 ± 0.011	0.870 ± 0.037	0.838 ± 0.023
h	$0.6859^{+0.0073}_{-0.0074}$	0.6869 ± 0.0071	0.724 ± 0.030	0.699 ± 0.014
t_0/Gyr	13.772 ± 0.036	13.77 ± 0.036	13.718 ± 0.052	13.753 ± 0.040
$f(z = 0.32)$	$0.6777^{+0.0087}_{-0.0084}$	$0.6764^{+0.0083}_{-0.0082}$	0.6800 ± 0.0090	$0.6789^{+0.0088}_{-0.0087}$
$f(z = 0.57)$	$0.7699^{+0.0073}_{-0.0071}$	$0.7688^{+0.0070}_{-0.0069}$	0.784 ± 0.012	$0.7754^{+0.0099}_{-0.0098}$

This paper has been typeset from a TEX/LATEX file prepared by the author.